# XAFS SPECTROSCOPY CHARACTERIZATION OF MIXED SILICA – ZIRCONIA OXIDES

# *INDEX*

# *Abbreviations and acronyms used in the text*

| | |
|---|---|
| BPO | Dibenzoylperoxide |
| XANES | X-ray-Absorption Near Edge Structure |
| EXAFS | Extended X-ray-Absorption Fine Structure |
| $E_K$ | Kinetic Energy |
| HASYLAB | Hamburger Synchrotronstrahlungslabor |
| MAA | Methacrylic acid |
| MAMTES | [(Methacryloxy)methyl]triethoxysilane |
| NMR | Nuclear Magnetic Resonance |
| OMc | Methacrylic group |
| TEM | Transmission Electronic Microscopy |
| THF | Tetrahydrofuran |
| XRD | X-Ray Diffraction |
| $Zr(O^nPr)_4$ | Zirconium(IV)-n-propoxide |

# *Used symbols*

| | |
|---|---|
| e | Electron charge |
| E | energy of the X-ray photon |
| $E_0$ | Energy of the Edge |
| $F_j(k)$ | Backscattering amplitude |
| $I_0$ | Initial intensity |
| I | Final intensity |
| $m_e$ | Electron mass |
| Mod (r) | Modulo function |
| $N_j$ | Neighbouring atoms |
| $r_j$ | Distance between the absorber atom and backscatterers j |
| $S_i(k)$ | Amplitude reduction of the central atom |
| $\mu$ | Absorption coefficient |
| $\mu_0$ | Background absorption |
| $\chi(k)$ | EXAFS function |
| h | Planck constant |
| $\rho$ | State density available for the electron |
| T | Incident photon frequency |
| $M_{if}$ | Dipole matrix element related to the transition of the electron |
| p | Momentum operator |
| *e* | Electric field vector of the X-ray photon |
| $\Psi_i$ | Wave function of the initial state |
| $\Psi_f$ | Wave function of the final state |

| | |
|---|---|
| $\Psi_{out}$ | Wave function of the outgoing photoelectron |
| $\Psi_{sc}$ | Backscattered wave function |
| $\sigma_j$ | Debye-Waller factor |
| $\phi_{ij}(k)$ | Phase shift |
| $\lambda_j$ | Electron mean free path |

# Introduction

The aim of this work is to study the local structure of $ZrO_2$-$SiO_2$ mixed oxides obtained from hybrid inorganic-organic materials as precursors. The hybrid materials were synthesised with different Si/Zr atomic ratios, annealed in microwave or in muffle oven to investigate the compositional and microstructural evolution of the materials. In the present study the Extended X-ray Absorption Fine Structure Spectroscopy (EXAFS) has been used. In fact, by using this tecnique the metal ions, the coordination numbers, the nature of the neighbouring atoms and the interatomic distances can be determined. In addition, the X-ray Absorption Near Edge Structure (XANES) provided a further insight about coordination geometry and oxidation state of the metal ions. With EXAFS and XANES spectroscopies, the influence of the Si/Zr molar ratio, annealing temperature and method of thermal treatment on the local enviroment of Zr in the mixed oxide materials is studied.

The materials have been prepared by copolymerisation of the organically modified oxozirconium cluster $Zr_4O_2(OMc)_{12}$ (OMc = methacrylate) with (methacryl-oxymethyl)triethoxysilane (MAMTES). This copolymerisation allows the stable anchoring of the clusters to the silica network formed as consequence by the hydrolysis and condensation reactions of the alkoxy groups. The obtained inorganic-organic hybrids have been calcined at different temperatures to yield the Zr-Si-O mixed oxides. The use of hybrid materials, characterised by a homogeneous distribution of the cluster in the polymeric network, has proved to give an uniform dispersion of zirconia particles in the silica matrix, avoiding agglomeration and phase separation phenomena.
The preparation of the hybrid inorganic-organic materials is in details described in chapter 1.

The theory of EXAFS spectroscopy as well as the analysis and discussion of the measured EXAFS spectra is presented in chapter 2. The effects of sample composition, annealing temperature, and method of thermal treatment are also

discussed. A detailed description of the experiments performed is reported in chapter 3, whereas the obtained results are summarised in chapter 4.

# Chapter 1

## 1.0 Importance of the $SiO_2$-$ZrO_2$ mixed oxides

The interest devoted to binary zirconia-silica oxides can be traced back to their enhanced catalytic, mechanical, electronic, thermal properties. These materials can be used as coatings, fibres, catalysts and high-refractive-index glasses. Zirconia and silica systems are used as catalysts [Itoh, M. *et al.* (1974), Miller, J.B. *et al*. (1996)], and as supports for catalysts and for further functionalisations [Soled, S. *et al.* (1992)]. In fact, zirconia is characterised by an interesting catalytic activity due to the presence of several acid sites. Unfortunately, its use is limited by the high cost and low specific surface area. To overcome this problem, the dispersion of the zirconia in the silica matrix has been used [Dang, Z. *et al.* (1995)], thus obtaining a highly catalytic activity in the selective formation of isobutene from synthesis gas (CO and $H_2$) [Moon, S.C. *et al.* (1997), Feng, Z.T. *et al.* (1994)], in the dehydratation of isopropanol and n-butanol [Lopez, T. *et al.* (1999)] and in the dehydrogenation of cycloesanol [Bosman, H.J.M. *et al.* (1994)].

The structure of mixed zirconia-silica oxides is very interesting because zirconium cannot substitute silicon, due to the different atomic radius and coordination number between these two elements. Only one well characterised crystallline compound, namely zircon ($ZrSiO_4$), is known [Hazen, R. M. *et al.* (1979)].

## 1.1 Chemical approach to mixed oxides

The preparation of mixed zirconia-silica glasses by melt quenching is highly demanding because of the required high melting temperatures [Evans, A. M. *et al.* (1980)]. These binary systems have been recently prepared by chemical solution deposition [Neumayer, D. A. *et al.* (2001)] and by a conventional sol–gel process starting from the corresponding alkoxides [Mountjoy, G. *et al.* (2003), Miller, G. B. *et al.* (1997)].

In particular, many efforts have been dedicated to the incorporation of host particles in a silica network, achieved by the sol–gel process [Brinker, C. J. *et al.* (1990)]. This powerful synthetic method, mainly based on the hydrolysis and condensation of metal alkoxides, provides a reliable route to oxide materials as well as to inorganic–organic hybrid materials [Sanchez, C. *et al*. (1992), Sanchez, C. and Toledano, P. *et al*. (1992)]. To avoid the disadvantages associated with the formation of inhomogeneities in the composite materials, which are not favourable for many applications, the use of organofunctional silanes of the type $R_nSi(OR')_{4-n}$ ($1 < n < 4$) as coupling agents has gained growing attention [Sanchez, C. *et al*. (1992)]. The general OR' (R' = Me, Et, Pr, etc.) alkoxy group undergoes, in the presence of water and of a catalyst, sol–gel hydrolysis and condensation reactions to give the silica network. The organofunctional group R, typically an acrylic or methacrylic moiety, can be instead chemically bonded to a polymer chain to afford a homogeneous intermixing of the two networks.

This route is well suited to homogeneously graft metal oxide precursors which, upon calcination, gives binary oxide systems of the type $MO_x$–$SiO_2$ in which the guest metal oxide is evenly dispersed in the silica matrix. In recent years [Armelao, L. *et al.* (2005)] we have used hybrid material as "components precursors" for the obtainment of highly uniform dispersion of guest oxides in silica host matrix.

By using this approach, which is in detail described in chapter 3, an even dispersion of zirconia in silica has been obtained. The controlled heating of the materials yielded, according to the annealing temperature, amorphous or crystalline phases of the $ZrO_2$-$SiO_2$ system.

# Chapter 2

## 2.0 Theory of EXAFS Spectroscopy

Extended X-ray Absorption Fine Structure (EXAFS) spectroscopy is a useful method for determining the local structure around a specific atom in disordered systems [Bertagnolli, H. *et al.* 1994]. This technique provides information about the coordination number, the nature of the scattering atoms surrounding a particular absorbing atom, the interatomic distance between the absorbing atom and the backscattering atoms and the Debye-Waller factors (structural disorder) of the different shells.

This structural determination of the local structure is limited to a distance given by the mean free path of the photoelectron in the condensed matter, which is between 5 and 10 Å radius from the element. These characteristics make EXAFS a powerful structural local probe, which does not require a long-range order. It is an important technique in several fields of natural sciences, from earth sciences to biochemistry. Since EXAFS is a technique selective for a particular element and sensible only for a short-range order, it is one of the most appropriate spectroscopy to be applied in the following cases:

- amorphous solids, *e.g.* ceramics,
- liquids, *e.g.* solutions of ionic compounds or gels which cannot be studied by X-Ray diffraction.
- biomolecules, *e.g.* solutions of metalloproteins,
- homogeneous and heterogeneous catalysts.

Furthermore, EXAFS does not require any particular experimental conditions, such as vacuum (at least in principle).

The measurements were carried by using high energy X-rays, which are normally generated by synchrotron radiation sources.

Measurements taken under in situ conditions are of critical importance in the case of heterogeneous catalysts in order to understand their behaviour during catalysis and in studying temperature and pressure induced changes. On the other hand, there are some problems associated with this spectroscopy. First, the necessity of synchrotron light as a source, which is easily available. Second, the use of simulation and best-fit procedures which are time-consuming and sometimes give ambiguous or unreliable results. However, if the system under study is properly investigated, EXAFS is able to supply useful and even essential information.

**Origin of the EXAFS signal**

Although the effect on which X-ray absorption spectroscopy (EXAFS spectroscopy) is based has been known for about 70 years, up until 20 years ago it had not found any application. The reasons for this were the lack of an efficient X-ray sources and of a suitable theoretical description. With the advent of synchrotron radiation, the situation has completely changed [Bertagnolli, H. *et al* (1994)].

EXAFS refers to the oscillatory variation of the X-ray absorption as a function of photon energy beyond an absorption edge. The absorption, in terms of absorption coefficient ($\mu$), can be determined from a measurement of the attenuation of X-rays upon their passage through a material.

The X-ray absorption coefficient for an atom ($\mu$) is directly proportional to the probability of absorption of one photon and is a monotonically decreasing function of energy. It shows several discontinuities which are known as absorption edges (figure 2.2): they occur when the energy of the incident photons equals the binding energy of one electron of the atom and are classified with capital letters (K, L, M...) according to the principal quantum number of the electron in the ground state ($n$ = 1, 2, 3...). There are many tables describing the energy position of all existing absorption edges for all types of atoms.

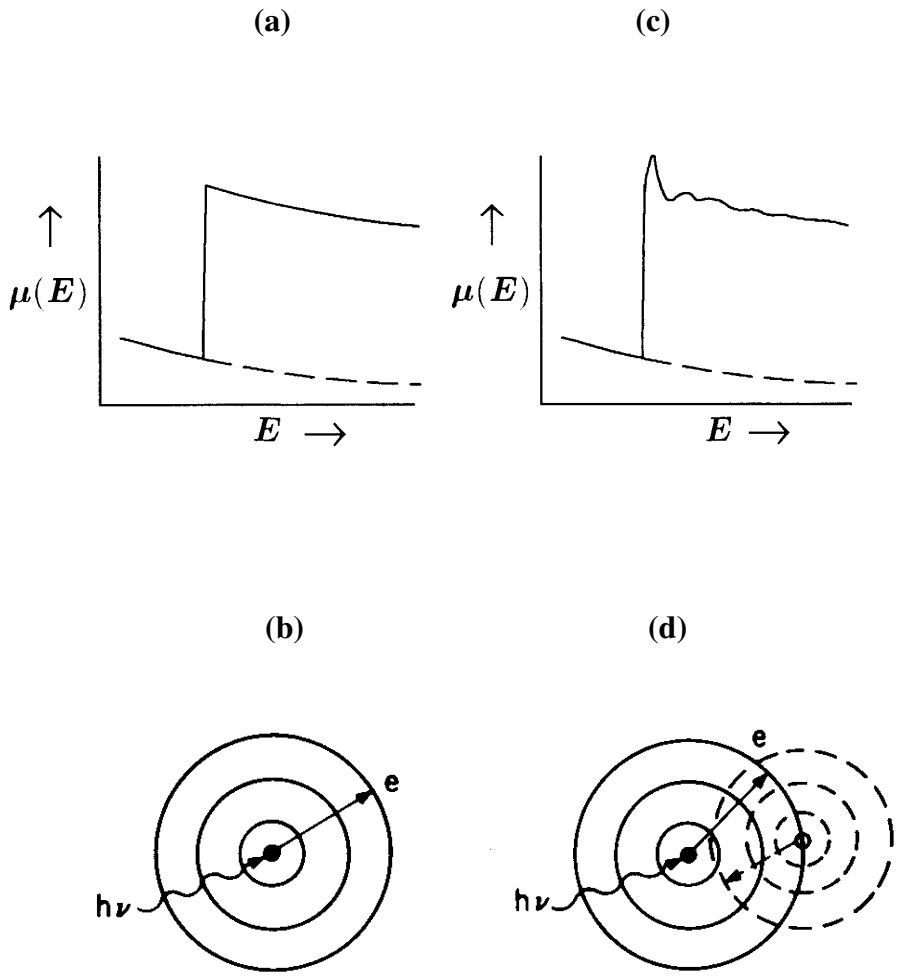


**Figure 2.1**: The absorption coefficient $\mu$(E) as a function of photon energy E for an isolated atom (a) and (b) and for an atom surrounded by backscattering atoms (c) and (d).

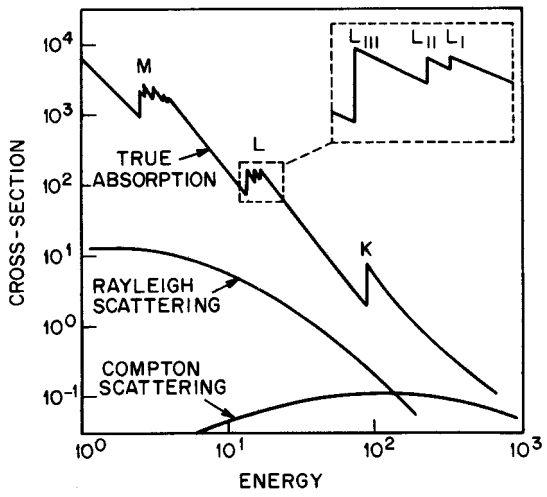


**Figure 2.2**: Example of an absorption spectrum.

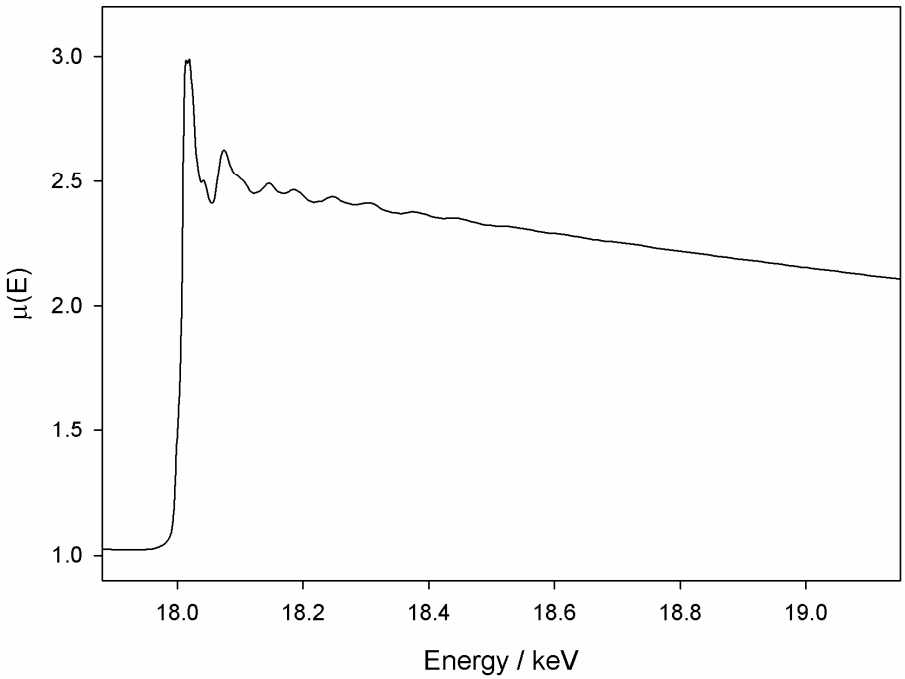


**Figure 2.3**: Example of an absorption spectrum for tetragonal $ZrO_2$ (K edge) showing EXAFS signal.

The dependence of the linear absorption coefficient ($\mu$) on the photon energy ($E$) is shown in figure 2.1. $\mu(E)$ decreases with increasing $E$ of the incident X-rays until a threshold is reached at which the energy is sufficient to remove an electron from an inner shell. At this threshold, $\mu(E)$ increases abruptly and beyond this point, $\mu(E)$ resumes a steady decrease. The curve shown in figure 2.1a is typical only for isolated atoms. When other atoms are in the vicinity of the absorbing atom, $\mu(E)$ shows small oscillations up to about 1000 eV above the absorption edge, as depicted in figure 2.1c. The probability for absorption of an X-ray photon by an electron of an inner shell is dependent on the initial and final states of the excited electron. The initial state is that of the core electron, while the final state is more difficult to describe. The absorption of X-ray radiation generates a photoelectron that can be considered as a spherical wave originating from the absorbing atom (figure 2.1b). This wave is then backscattered by the neighbouring atoms which become scattering centers of the photoelectron wave (figure 2.1d) [Krishnan, V. *et al.* (2004)].

The final state of the photoelectron can be described by the sum of the original and scattered waves. This leads to an interference phenomenon that modifies the interaction probability between core electrons and incident photons. Constructive

interference increases while destructive interference decreases the absorption coefficient of the atom [Vlaic, G. *et al* (2004)].

If the absorbing atom is isolated in space like in the figure 2.1b, the photoelectron propagates as an unperturbed isotropic wave, but in most cases there are many other atoms around the absorber. This interference phenomenon, for a given energy of the photoelectron, depends on the distance between emitting and scattering atoms, and their atomic numbers.

Before the edge, there may appear absorption peaks due to excitation of core electrons to some bound states. Therefore, this pre-edge region contains information about the energetics of virtual orbitals, the electronic configuration and the site symmetry [Teo, B.K. *et al.* (1986), Teo B.K. *et al.* (1979)].

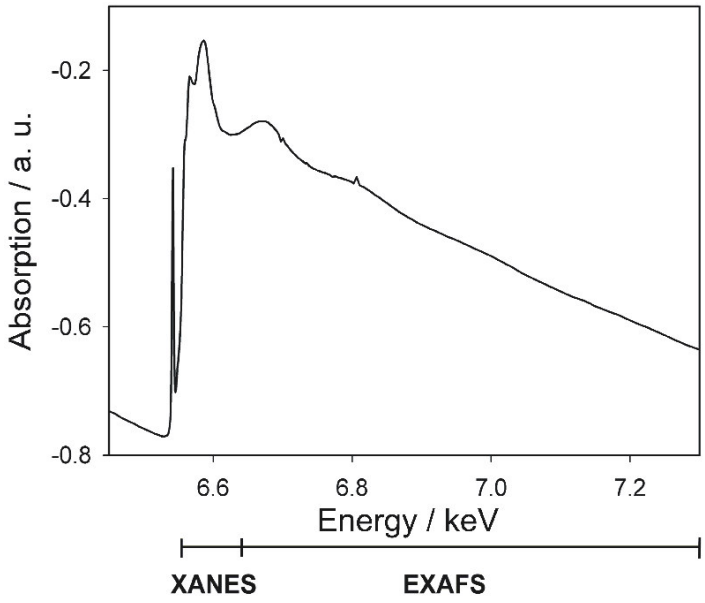


**Figure 2.4:** Example of a near edge (XANES) region and far-edge (EXAFS) region for an absorbing center.

The region at 30 eV before the edge to about 40 eV after the edge is the X-ray absorption near edge structure (XANES) area (figure 2.4). Its shape is dependent on effects such as many-body interactions, multiple scatterings, distortion of the excited state wave function by the coulomb field, band structures, etc. The edge position contains information about the oxidation state of the absorbing atom whereas, as mentioned the EXAFS region provides information on the coordination number, the nature of the scattering atoms surrounding the absorbing (excited) atom, the interatomic distance between the absorbing atom and the backscattering atoms and Debye-Waller factor which accounts for the disorder

due to the static displacements and thermal vibrations [Bertagnolli *et al* (1994)]. Thus, the measurement of the energy dependence of the X-ray absorption coefficient can be used to determine the local environment around the element, which absorbs the X-rays. Since the positions of the K and L edges are dependent on the element under investigation, the suitable choice of incident X-ray energies makes it possible to excite a particular element and hence to probe its environment. The elements suitable for EXAFS study are determined by the spectral region of the X-ray source. For lighter elements it is necessary to employ soft X-rays and high vacuum techniques.

An incident photon is able to extract a core electron if its energy is equal to or greater than the edge energy. The ejected electron is called photoelectron and it has the characteristics of both a particle and a wave. Its kinetic energy ($E_K$) is given by:

$$E_K = E - E_0 \quad (2.0)$$

where E is the energy of the X-ray photon and $E_0$ the energy of the edge. In order to determine the relationship between the quantities characterizing the neighborhood environment around the absorbing atom and the X-ray absorption coefficient μ(E), it is necessary to correct and normalize the modulation of μ(E) for the background absorption $\mu_0$(E) using equation (2.1).

$$c(E) = \frac{\mu(E) - \mu_0(E)}{\mu_0(E)} \quad (2.1)$$

Dividing by $\mu_0(E)$ normalizes the signal. Such a definition means that $\chi(E)$ contains only the oscillatory part of the absorption coefficient.

The next step is to convert $\chi(E)$ into the function $\chi(k)$, where $k$ is the magnitude of the photoelectron wave vector which is calculated according to equation (2.0) from the energy $E$ of the incident X-ray photon and the position of the absorption edge $E_0$.

$$k = \left[\frac{8p^2 m_e}{h^2}(E - E_0)\right]^{1/2} \quad (2.2)$$

Here, $m_e$ is the mass of the electron and $h$ is the Planck's constant. In order to extract structural information from experimental spectra, a simple analytical expression that relates the EXAFS signal to the structural parameters is required. To obtain a simplified EXAFS formula some approximations have to be assumed. First of all, the dipole approximation, which describes the interactions among core electrons and hard X-ray photons. This approximation allows to express the absorption cross-section as:

$$P_{jf} = \frac{2\pi^2 e^2}{m_e^2 \omega} \left| M_{if} \right|^2 \rho(E_f) \qquad (2.3)$$

where i and f stand for initial and final states of the electron respectively, $e$ and $m_e$ are its charge and mass, $\rho(E_f)$ is the state density available to the electron (it is considered as a free electron so there is a continuous distribution of states), $T$ is the incident photon frequency and $\left| M_{if} \right|$ is a dipole matrix element related to the transition of the electron from i to f state.

$$\left| M_{if} \right| = \left\langle \psi_f \left| p \cdot e \right| \psi_i \right\rangle \qquad (2.4)$$

where $p$ is the momentum operator, $e$ is the electric field vector of the X-Ray photon, $\Psi_i$ and $\Psi_f$ are wave functions for initial and final states. The most difficult issue during the analysis is to obtain a good expression of the final state wave function. This can be done by choosing a proper approximation for the potential function that describes the system. In most cases, this problem is overcome by using the "muffin-tin" approximation. Moreover, the single electron approximation and the sudden approximation are introduced. Under these conditions, $\Psi_f$ depends on the absorbed photon energy and can be written as a linear combination of two terms: the wave function for the outgoing photoelectron from the excited atom $\Psi_{out}$, and a perturbing term $\Psi_{sc}$ which represents the backscattered wave.

At this point, keeping in mind that the absorption coefficient is proportional to $P_{if}$, it is possible to write a theoretical expression of the EXAFS signal:

$$\chi(k) = \frac{\langle \psi_{out} + \psi_{sc} | p\Box e | \psi_i \rangle}{\langle \psi_{out} | p\Box e | \psi_i \rangle} - 1 \qquad (2.5)$$

Starting from this formula and with several mathematical transformations and minor physical approximations, it is finally possible to write an EXAFS analytical expression like the one suggested by E. A. Stern [Stern, E.A. *et al.* (1974)]:

$$c(k) = \sum_j N_j \times S_i(k) \times F_j(k) \times \exp\left[-2\times\sigma_j^2\times k^2\right] \times \exp\left[\frac{-2\times r_j}{l_j(k)}\right] \times \frac{\sin\left(2\times k\times r_j + f_{ij}(k)\right)}{k\times r_j^2} \qquad (2.6)$$

Here $F_j(k)$ is the backscattering amplitude from each of the $N_j$ neighbouring atoms of the $J^{th}$ type with a Debye-Waller factor of $\sigma_j$ (to account for the thermal vibration) and static disorder (assuming Gaussian pair distribution) and at the distance $r_j$ away. $\phi_{ij}(k)$ is the total phase shift experienced by the photoelectron. The term $\exp\left[-2\times\sigma_j^2\times k^2\right]$ is due to anaelastic losses in the scattering process (due to neighbouring atoms and the medium in between) with $l_j$ being the electron mean free path. $S_i(k)$ is the amplitude reduction at the central atom (denoted by i).

It is clear that each EXAFS wave is determined by the amplitude ($N_j \times S_i(k) \times F_j(k)$), modified by the reduction factors $S_i(k)$, $\exp\left[-2\times\sigma_j^2\times k^2\right]$, and $\exp\left[\frac{-2\times r_j}{l_j(k)}\right]$, and the $1/k\,r_j^2$ distance dependence, and the sinusoidal oscillation which is a function of interatomic distances ($2\times k\times r_j$) and the phase shift ($f_{ij}(k)$).

Equation 2.6 is valid in the case of non-oriented samples (crystalline powders, solutions and gases) and/or in the case of a non-polarized light source. Using polarized light, like synchrotron radiation with monocrystals, implies a correction of the equation: it must be multiplied by 3 $\cos^2\Theta$ where $\Theta$ is the angle between the absorber scatterer axis and the polarization direction. Non-oriented samples do not require this correction, because the angle is isotropically distributed in space. Summarising, this equation relates the EXAFS function $\chi(k)$, to the quantities that characterize the local environment of the absorbing atom, i.e. atom type of the backscatterers, coordination number, interatomic distances and Debye-Waller factors [Lytle, F.W. *et al.* (1975); Sayers, D.E. *et al* (1983)].

For analysis, the EXAFS function $\chi(k)$ is weighted with $k^n$ (n=1-3) in order to compensate the decrease of $\chi(k)$ with increasing $k$ (figure 2.5). This decrease is caused by the functional form of the backscattering amplitude $F_j(k)$ and the factor $exp(-2\sigma_j^2 k^2)$.

The EXAFS function in k space contains all necessary structural information; however, it is not readily visualized. Fourier transformation of the EXAFS function yields a radial distribution function and therefore indicates the distribution of the backscatterers in real space (figure 2.5 equation 2.7).

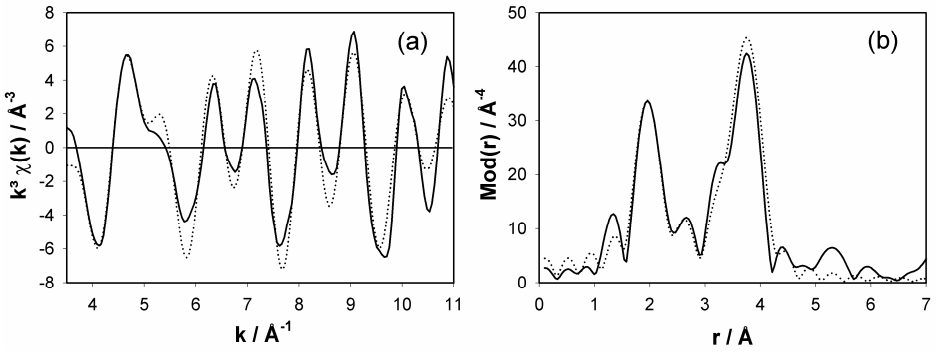


**Figure 2.5:** Experimental (solid line) and theoretical (dotted line) EXAFS functions weighted with $k^3$ and their corresponding Fourier transform for tetragonal $ZrO_2$.

$$F(r) = \frac{1}{\sqrt{2\pi}} \int_{k_{\min}}^{k_{\max}} \chi(k) \cdot k^n \cdot w(k) \cdot e^{2ikr} dk \qquad (2.7)$$

$$Mod(r) = \sqrt{\mathrm{Re}^2[F(r)] + \mathrm{Im}^2[F(r)]} \qquad (2.8)$$

The modulus of F(r) shows maxima at $R_j = r_j - \alpha_j$ which are shifted by $\alpha_j \approx 0.2 - 0.3$ Å to smaller distances due to the total phase shift [Stern, E. A. *et al.*(1975), Teo, B. K. *et al.* 1986)]. Additionally, it should be mentioned that the Mod(r) functions shown in chapters 2 and made with Excurve 98 are phase-shift corrected. Therefore, the correct interatomic distances are shown for the first coordination shell and all further shells of this element. In order to reach this, before and/or during the Fourier transformation, the backscattering amplitude and the total phase shift of the first backscatterer are considered. The maxima of other elements are still shifted because of the other backscattering amplitude and the

deviating phase shift function. However, these deviations are usually smaller than the peak width [Gurman, S. J.*et al.* (1990)].

**Beamline**

The EXAFS measurements of the examined substances were performed at the beamline X1 at HASYLAB, DESY (Hamburg). In figure 2.6a the experimental setup of an EXAFS measurement in transmission mode is schematically shown. The radiation source is the synchrotron ring, in which electrons or positrons moving at the speed of light are forced by bending magnets on a circular path. The white synchrotron radiation produced thereby possesses a high intensity over a large spectral range, is strongly focused and polarized in the ring level. By Wigglers or Undulators, special arrangements of alternatingly polarized magnets within the synchrotron ring, the intensity of the synchrotron radiation can be strengthened in comparison to normal bending magnets.

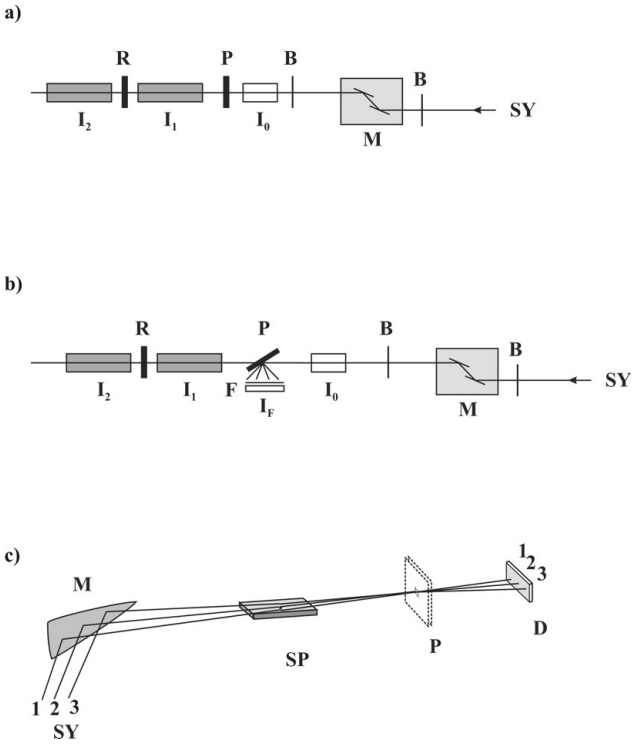


**Figure 2.6**: Experimental setup for transmission (a), fluorescence (b) and energy-dispersive (c) EXAFS measurements (SY-synchrotron radiation, B-slit, M-monochromator, P-sample, R-reference material, $I_0$, $I_1$, $I_2$-ionization chambers, F-filter, 1,2,3-beam paths, D-detector (diode array), SP-mirror).

The X-ray absorption spectroscopy measures the X-ray absorption coefficient μ as a function of the photon energy E. The most common technique involves the direct measurement of $\mu(E)$. In order to obtain monochromatic X-rays, a continuous spectrum is used. As previously explained, the most suitable source is synchrotron radiation, but X-rays from conventional X-ray sources can also be employed as well [Thulke, W. *et al* (1983), Tohji, K *et al* (1989)]. In this case, the intensity is lower by a factor of $10^3$. The absorption coefficient is found by measuring the intensity of the X-rays before and after the sample. The energy of the incident radiation is adjusted by a stepwise change of the incident angle of the monochromator, which reflects radiation of wavelength $\lambda$ according to the Bragg's law [Stout, G.H. *et al* (1989)] given in equation (2.9),

$$n\lambda = 2d \sin \theta \qquad (2.9)$$

Here, $\lambda$ refers to the wavelength of the incident X-rays, d is the spacing between the lattice planes of the crystal, $2\theta$ is the scattering angle and n is the order of diffraction (n = 1,2,3,….). According to this law, a double crystal monochromator, with the second crystal at a slightly detuned angle with respect to the first one, selects a beam of wavelength $\lambda$, while simultaneously suppressing beams with wavelengths $\lambda/2$, $\lambda/3$, etc.

The monochromatic beam passes through a slit system and meets afterwards the first ionization chamber, in which the output intensity $I_0$ is determined. Thereupon, the sample and the second ionization chamber follow, which detects the weakened intensity $I_1$ (fig. 2.6a). Additionally, the spectrum of a reference sample (mostly a metal foil) is measured between the second and third ionization chamber in order to make possible an exact energy calibration. Depending on the energy of the absorption edge, the ionization chambers are filled with nitrogen, argon or mixtures of these gases. The ratio of both gases should be selected in such a way that 10 % of the incident radiation is absorbed in the first ionization chamber, 50 % in the second and the rest in the third ionization chamber [Lee, P. (1981)].

Data is collected by measuring how the beam intensity decreases as it passes through the sample while scanning energy using a crystal monochromator.

Experimental spectra are usually recorded by scanning energy from about 200 eV below the explored edge to 1000 eV above it. Energy steps can be of 0.1–2.0 eV, depending on the energy interval and the experimental setup.

As it is known, the Lambert-Beer law relates intensities $I_0$ and I to the absorption coefficient:

$$\ln \frac{I_0}{I} = \mu x \quad (2.10)$$

The intensity measured by the ionization chambers is recorded as photon counts by a photomultiplier (figure 2.7).

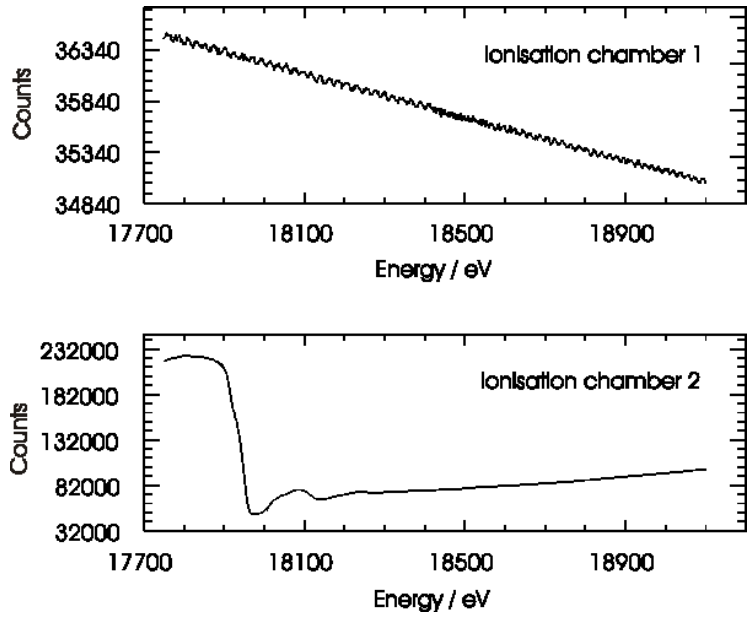


**Figure 2.7:** The spectra counts for the sample ZS10.0_mf1000 obtained in transmission mode using two chambers as detectors.

Since the absorption of X-rays is linked to the creation of an electron vacancy, it is possible to use all subsequent decay processes to determine the absorption coefficient. An electron from an outer shell can fill the vacancy, accompanied by the emission of fluorescence radiation. The fluorescence yield increases with increasing atomic number and this process has the advantage that the background radiation can be removed by using suitable filters, which increases the sensitivity of the method. A typical setup for fluorescence measurements is shown in figure

2.6b. In general, the emitted fluorescence is measured at right angle to the incident beam: the sample is therefore rotated by 45°. Fluorescence mode measurements are performed whenever the concentration of the absorbing species in the sample is low. Typical measurement times for an X-Ray absorption spectrum are 20-60 minutes, when synchrotron radiation is used. Rapid rotation of the monochromator crystals can reduce these times to a few seconds however, the experimental effort is increased drastically [Frahm, R. et al (1989)]. This technique is used to monitor fast reactions. The acronym for this measuring technique is QEXAFS (Q = quick). The continuous X-ray spectrum can also be used directly (2.6c). After the passage through the sample it is split up by Bragg reflection when incident in a spherical type of curved crystal. The intensities are measured by a diode array detector [Hagelstein, M. et al (1989), Fontaine, A. et al (1988)]. This measurement principle is depicted in the previous figure (Figure 2.6c) and is called DEXAFS (D = dispersive). The detection of the emitted Auger electrons during the absorption process also yields structural information. This method can be employed where the other methods fail. Due to the small mean free wavelength of the emitted electrons (~100 Å), the Auger method is especially suited for the study of surfaces, and the related method is known as SEXAFS (S = surface) [Koningsberger, D.C.; Prins, R. et al (1988)].

Because of the angular rotation of the crystals inside the monochromator, the beam can shift up or down. Light must pass through the sample always at the same position, so either the sample follows the beam by placing it on a micrometric table, or it is necessary to change the monochromator mechanism to obtain a fixed beam.

## 2.1 XANES of the monoclinic and tetragonal phases of crystalline $ZrO_2$

Tetragonal and monoclinic phases represent two of the three well-known crystalline modifications of zirconium dioxide, which are related in this way [Gmelins Handbuch der anorganischen Chemie (1973)]:

$$ZrO_2 \text{ (monoclinic)} \underset{1100°C}{\leftrightarrows} ZrO_2 \text{ (tetragonal)} \underset{2350°C}{\leftrightarrows} ZrO_2 \text{ (cubic)}$$

Crystallisation of monoclinic zirconia generally occurs at about 450°C [Gmelins Handbuch der anorganischen Chemie (1973)]. For pure zirconium dioxide, the transformation of the monoclinic into the tetragonal form takes place at around 1100°C. As we can see from the XANES spectra of the two references (figure 2.8), tetragonal and monoclinic $ZrO_2$ exhibit distinct features [P. Li *et al.* (1993)]. First of all, there is no detectable edge shift among the spectra. This is consistent with the notion that the valence of Zr in these samples remains the same. Furthermore, the tetragonal form has a white line (which is the first maximum after the edge step) characterized by a double peak, whereas the monoclinic form has mainly a single peak. The shape of the main absorption peak represents transitions to np continuum states and "shape resonances" of the metal atom environment [Mountjoy e*t al.* (2000)]. The edge width of the XANES spectrum is commonly defined as the full width at half maximum of the main peak in the first derivative.

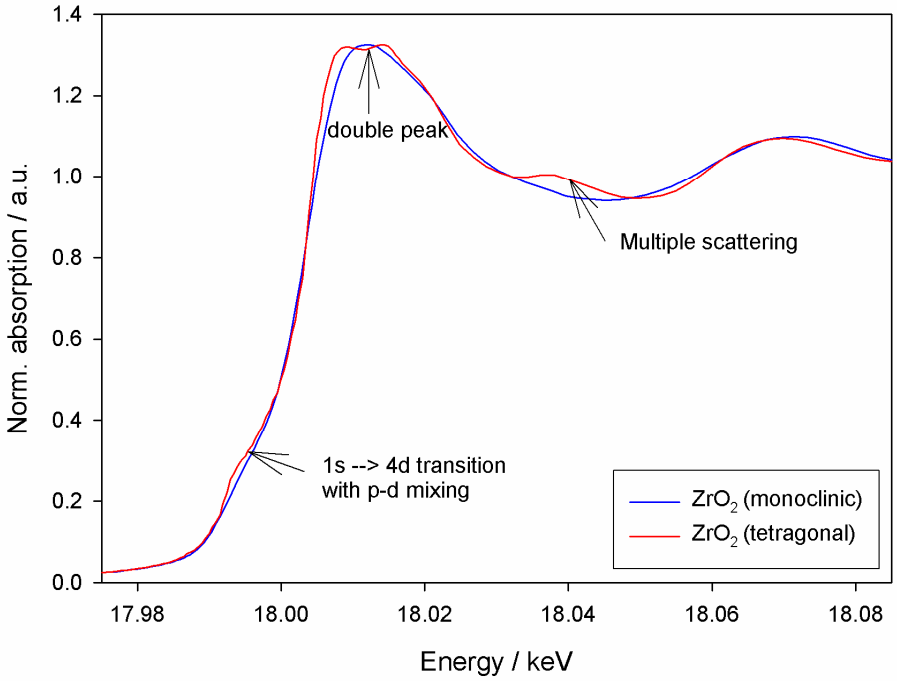


**Figure 2.8:** XANES spectra of monoclinic and tetragonal $ZrO_2$.

As can be seen from the first derivatives of the XANES spectra (figure 2.9), the monoclinic polymorph exhibits a broader edge width with respect to the tetragonal one.

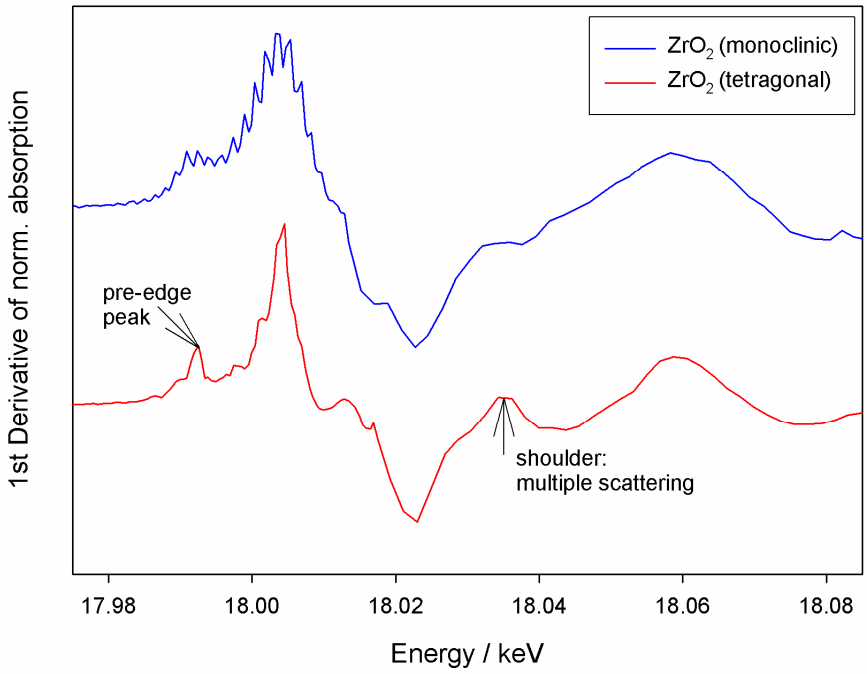


**Figure 2.9:** First derivatives of the XANES spectra of monoclinic and tetragonal $ZrO_2$.

The edge width is a measure of the splitting of the degenerate energy levels and an indicator of the coordination symmetry around the absorber atom. For highly symmetric coordination the edge width should be small [Srivastava, U.C. *et al.* (1973), Bart, J.C.J. *et al.* (1986)]. This is in agreement with the fact that monoclinic $ZrO_2$ has a less symmetric structure than the tetragonal modification (figure 2.10). As can be seen, each zirconium atom in tetragonal $ZrO_2$ is coordinated by 4 oxygen atoms at the same lower distance (2.08 Å) and 4 other oxygen atoms at a higher distance (2.37 Å). In contrast, monoclinic $ZrO_2$ exhibits a seven fold coordination with interatomic distances ranging from 2.05 Å to 2.29 Å [P. Li *et al.* (1993)]. Furthermore, each of the seven oxygen atoms has another Zr-O interatomic distances. However, these differences can not be seen in the models shown in figure 2.10.

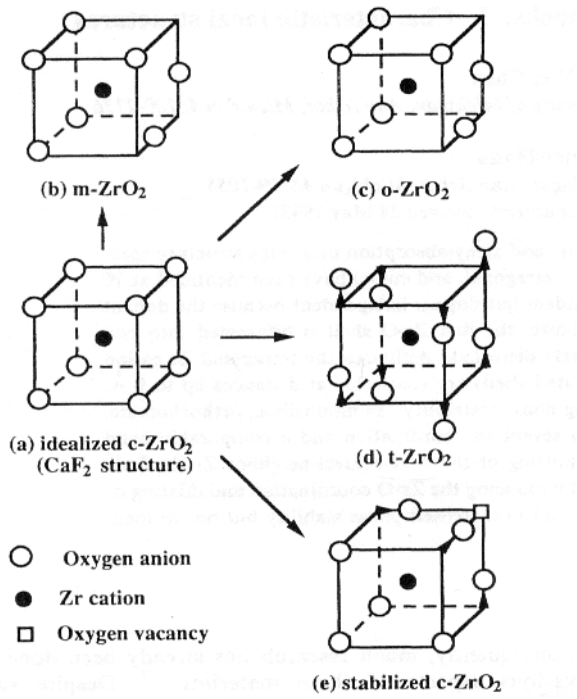


**Figure 2.10:** Schematic structure of polymorphic distortions in $ZrO_2$. Lower symmetry structure of monoclinic in comparison to tetragonal $ZrO_2$ can be clearly seen.

Alternatively, the edge width can be correlated with the overall covalent character of the metal-ligand bond [Zandiehnadem, F. *et al.* (1988)]. Therefore, the large edge width in monoclinic $ZrO_2$ is an indication for its higher covalency in comparison to tetragonal $ZrO_2$. Tetragonal $ZrO_2$ exhibits also a prominent shoulder around 18.037 keV that is not present in the monoclinic form. This peak corresponds to multiple scattering involving second nearest neighbour atoms or higher shells [Mountjoy e*t al.* (2000)]. The two forms can be distinguished also by the pre-edge peak at 17.993, which is much stronger for tetragonal $ZrO_2$. The same feature can be seen in the first derivative (figure 2.9). This pre-edge peak corresponds to a 1s $\rightarrow$ 4d transition which is only allowed if there is some p-d mixing. The intensity of this transition is stronger in compounds that are distorted from centrosimmetry. Since the Zr-O geometry in tetragonal $ZrO_2$ consists of two sets of non-equivalent tetrahedra and because tetrahedral geometries are known to enhance p-d mixing (due to the lack of centrosimmetry), a stronger transition is observed in tetragonal $ZrO_2$. All these three features (the pre-edge peak, the edge width and the shoulder around 18.037 keV) can be recognized more clearly in the first derivative (figure 2.9).

## 2.2 EXAFS of monoclinic and tetragonal crystalline $ZrO_2$

The EXAFS measurements were carried out at the Zr K-edge (17998 eV) in transmission mode at ambient conditions. The experimentally determined and theoretically calculated EXAFS spectra of monoclinic and tetragonal $ZrO_2$ are shown in figure 2.11 and 2.12 and the obtained structural parameters are summarised in table 2.1 along with the corresponding XRD data.

The spectrum of monoclinic $ZrO_2$ was fitted with a three shell model. A first oxygen shell was found at the distance of 2.08 Å which is in good agreement with the XRD data [B. Bondars *et al* (1995)]. As already mentioned, monoclinic $ZrO_2$ has a low symmetry structure and the shell at 2.07 Å obtained from XRD analysis (table 2.1) is the averaged result of three oxygen atoms at three different distances. A second oxygen shell was fitted at the distance of 2.23 Å. As for the first one, the XRD value at 2.22 Å (table 2.1) is an averaged value combining four oxygen atoms at four different distances. Additionally, a zirconium shell with a coordination number of 7 was fitted at the distance of 3.48 Å. This is in good agreement with the average distance (3.46 Å) of the first three Zr shells weighted according to their coordination number. It should also be noticed that the second Zr shell at 3.46 Å obtained from XRD analysis (table 2.1) represents the average of five Zr atoms at three different distances. Consequently, the obtained high Debye-Waller factor of the third shell is explained by the fact that three shells were combined in one.

**Table 2.1:** Structural parameters for the references monoclinic and tetragonal $ZrO_2$ [B. Bondars *et al* (1995)].

| | A-Bs[a] | N[b] | r[c] [Å] | σ[d] [Å] | $E_f$ [e] [eV] | k-range [$Å^{-1}$] | Fit Index |
|---|---|---|---|---|---|---|---|
| **Monoclinic** | Zr – O<br>Zr – O<br>Zr – Zr | 3.0<br>4.0<br>7.0 | 2.08<br>2.23<br>3.48 | 0.050<br>0.074<br>0.120 | 7.23 | 3.5 – 11 | 28.18 |
| **Tetragonal** | Zr – O<br>Zr – O<br>Zr – Zr | 4.0<br>4.0<br>12.0 | 2.10<br>2.30<br>3.63 | 0.067<br>0.097<br>0.107 | 5.81 | 3.5 – 11 | 31.16 |
| **XRD (monoclinic) Averaged values** | Zr – O<br>Zr – O<br>Zr – Zr<br>Zr – Zr<br>Zr – Zr<br>Zr – Zr | 3<br>4<br>1<br>5<br>1<br>2 | 2.07<br>2.22<br>3.34<br>3.46<br>3.57<br>3.93 | | | | |
| **XRD (tetragonal) Averaged values** | Zr – O<br>Zr – O<br>Zr – Zr | 4<br>4<br>12 | 2.08<br>2.37<br>3.62 | | | | |

[a] absorber (A) – backscatterers (Bs), [b] coordination number N, [c] interatomic distance r, [d] Debye-Waller factor σ and [e] edge position (Fermi energy) relative to calculated vacuum zero $E_f$.

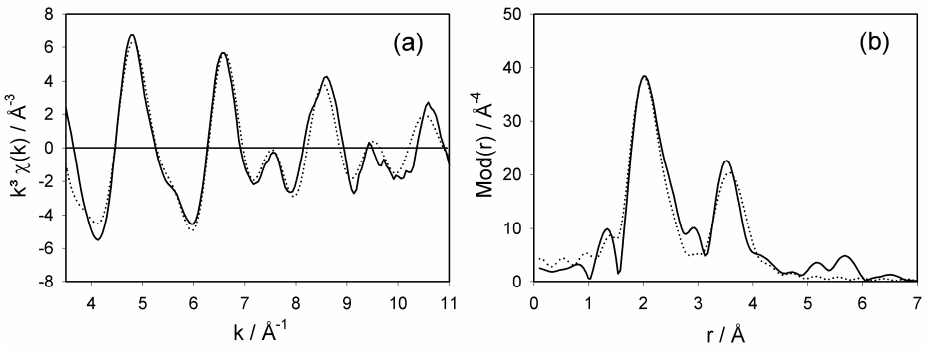


**Fig. 2.11:** Experimental (solid line) and theoretical (dotted line) EXAFS functions and their corresponding Fourier transform for monoclinic $ZrO_2$.

The spectrum of the tetragonal $ZrO_2$ was fitted according to literature values. The first shell comprised of 4 O-atoms was determined at the distance of 2.10 Å and the second shell consisting of 4 O-atoms was determined at the distance of 2.30 Å. Additionally, a Zr-shell with a coordination number of 12 was fitted at the distance of 3.63 Å. The distances are in good agreement with the XRD literature values [B. Bondars *et al.* (1995)] but there is a deviation of 0.07 Å for the second oxygen shell. This might be explained by the fact that two oxygen shells were combined to one peak. Moreover, characteristic of tetragonal $ZrO_2$ is a two-fold doublet structure in the χ(k)-function centred at about 6.8 and 8.5 $Å^{-1}$ (figure

2.12). If we compare the Fourier transforms of monoclinic and tetragonal $ZrO_2$ it can be seen that the oxygen peak of monoclinic $ZrO_2$ is broader and slightly higher than in the tetragonal spectrum.

The second peak which corresponds to the next nearest neighbours is highly sharp and strong. This can be attributed to the fact that cations in tetragonal $ZrO_2$ are in a simple, nearly face-centred-cubic (fcc) arrangement, while cations in other polymorphs all have severe distortions [P.Li *et al.* (1993)].

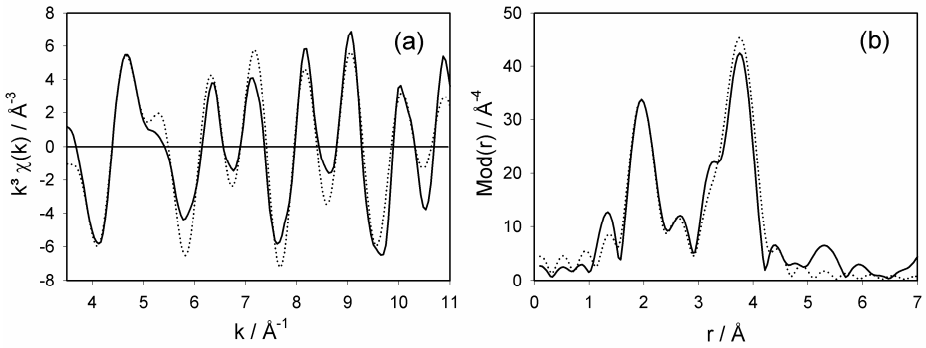


**Fig. 2.12:** Experimental (solid line) and simulated (dotted line) EXAFS functions and their corresponding Fourier transform for tetragonal $ZrO_2$.

## 2.3 Overview and nomenclature of the analysed samples

Different sequences of $ZrO_2$-$SiO_2$ mixed oxides were prepared at the "Dipartimento di Scienze Chimiche" at the University of Padova. As reported in chapter 1.1, the thermal treatments were carried out by conventional and microwave oven. The samples with Si/Zr molar ratios of 1.3 and 40.0 were annealed in a muffle oven for four hours. All other muffle oven samples were calcined for five hours. The calcination time for the microwave samples was always one hour.

All samples that were analysed by EXAFS spectroscopy are summarised in table 2.2 together with information on the Si/Zr molar ratio, annealing temperature and method of thermal treatment. The given Si/Zr molar ratios are based on the nominal composition of the synthesis solutions. For all samples, the same nomenclature was used: The label "ZS" indicates that the sample is a $ZrO_2$-$SiO_2$

mixed oxide, the following number represents the Si/Zr molar ratio and the labels "mw" and "mf" indicate whether the sample was calcined in a muffle or in microwave oven. The number at the end defines the annealing temperature of the materials [Armelao, L. *et al* (2005)].

**Table 2.2:** Overview and nomenclature of the analysed samples.

| Sample name | Si/Zr molar ratio | Annealing temperature (°C) | Method of thermal treatment |
|---|---|---|---|
| ZS1.3_as prepared | 1.3 | - | - |
| ZS1.3_mf500 | 1.3 | 500 | muffle |
| ZS1.3_mf700 | 1.3 | 700 | muffle |
| ZS1.3_mf900 | 1.3 | 900 | muffle |
| ZS1.3_mf1000 | 1.3 | 1000 | muffle |
| ZS40.0_as prepared | 40.0 | - | - |
| ZS40.0_mf500 | 40.0 | 500 | muffle |
| ZS40.0_mf700 | 40.0 | 700 | muffle |
| ZS40.0_mf900 | 40.0 | 900 | muffle |
| ZS40.0_mf1000 | 40.0 | 1000 | muffle |
| | | | |
| ZS5.0_mf600 | 5.0 | 600 | muffle |
| ZS5.0_mw600 | 5.0 | 600 | microwave |
| ZS5.0_mf800 | 5.0 | 800 | muffle |
| ZS5.0_mw950 | 5.0 | 950 | microwave |
| ZS5.0_mf1000 | 5.0 | 1000 | muffle |
| ZS20.0_mf600 | 20.0 | 600 | muffle |
| ZS20.0_mw600 | 20.0 | 600 | microwave |
| ZS20.0_mf800 | 20.0 | 800 | muffle |
| ZS20.0_mw950 | 20.0 | 950 | microwave |
| ZS20.0_mf1000 | 20.0 | 1000 | muffle |
| | | | |
| ZS12.5_mf1000 | 2.5 | 1000 | muffle |
| ZS10.0_mf1000 | 10.0 | 1000 | muffle |

## 2.4 XANES of the cluster and the "as prepared" samples

As can be observed from figure 2.13, the XANES spectrum of the sample ZS1.3_as prepared is similar to that of the $Zr_4O_2(OMc)_{12}$ (Zr4-cluster) and only a slightly lower intensity of the white line can be noted. This suggests that the

cluster retains its structure also once embedded in the hybrid matrix, as described in the experimental part. A different consideration should be assumed for the sample ZS40.0_as prepared, which does not show a similar behaviour. The edge width is significantly broader than in the Zr4-cluster and the height is lower, all features that will be later evidenced in the calcined samples. All these results indicate, in this case, that the cluster is modified in the silica matrix during the polymerisation process. It can be concluded that, at higher diluitions, the degradation of the cluster occurs, as already elsewhere reported [Feth, M. (2003)].

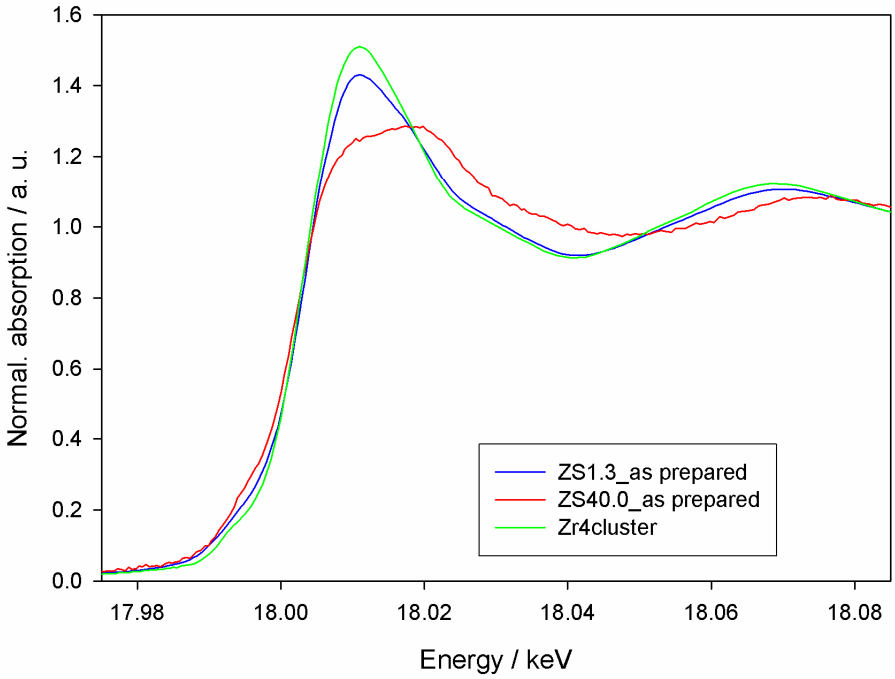


**Figure 2.13:** XANES spectra of $Zr_4O_2(OMc)_{12}$ cluster and the as prepared samples with a Si/Zr ratio of 1.3 and 40.0.

## 2.5 EXAFS of the cluster and the "as prepared" samples

The spectrum of the $Zr_4O_2(OMc)_{12}$ cluster was fitted (table 2.3, "fitting 1") according to literature values [Kickelbick G. *et al.* (2002)]. Coordination numbers were fixed to averaged values from single crystal X-ray analysis in order to obtain comparable values for the Debye-Waller factors. The experimentally determined and theoretically simulated EXAFS functions in *k* space and their Fourier transforms in real space for $Zr_4O_2(OMc)_{12}$ are shown in the figure 2.14. The determined structural parameters are listed in table 2.3. The fitting assumes a three shells model. The first shell containing 7.5 O-atoms was determined at the

distance of 2.20 Å and the second shell comprising 0.5 Zr-atoms was found at 3.33 Å. Additionally, a Zr-shell with a coordination number of two was fitted at the distance of 3.51 Å. The distances for the first shell are in accordance with the averaged values obtained from XRD [Kickelbick G. *et al.* (2002)], but the distance of the third shell is 0.15 Å shorter. The second shell of "fitting 1" is not significant because the enclosure of this shell improves the fit-index only by 1.3 per cent. Therefore, "fitting 2" is to be preferred.

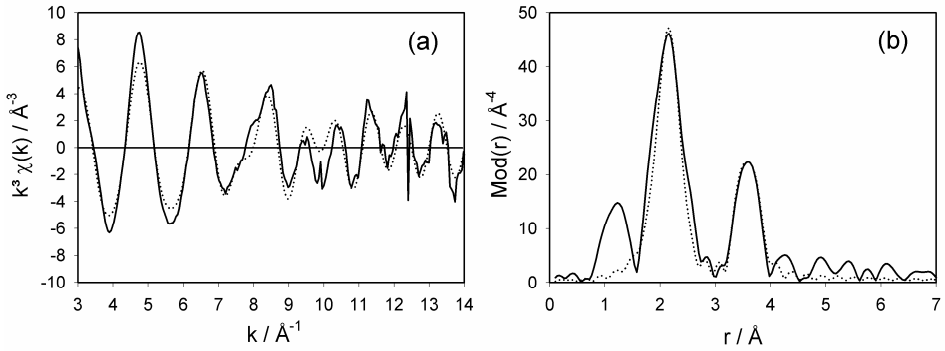


**Fig. 2.14:** Experimental (solid line) and simulated (dotted line) EXAFS functions and their corresponding Fourier transforms for $Zr_4O_2(OMc)_{12}$. ("Fittings 1").

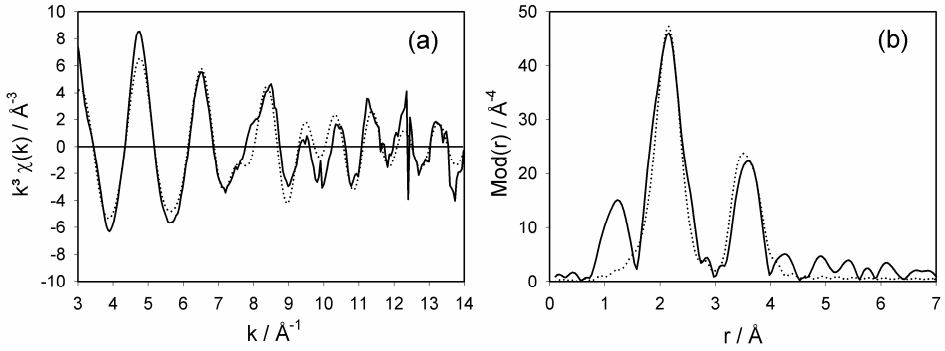


**Fig. 2.15:** Experimental (solid line) and simulated (dotted line) EXAFS functions and their corresponding Fourier transforms for $Zr_4O_2(OMc)_{12}$. ("Fittings 2").

In the fitting of the ZS1.3_as prepared sample, the coordination numbers of the oxygen and zirconium shells were set according to those of $Zr_4O_2(OMc)_{12}$. The experimentally determined and theoretically simulated EXAFS functions in *k* space and their Fourier transforms in real space for ZS1.3_as prepared are shown in the figure 2.16. The Debye-Waller factors of the two fitted shells with values of 0.107 Å and 0.084 Å are higher than those of the pure $Zr_4O_2(OMc)_{12}$. This can be explained by the higher disorder due to distortions of the cluster after

incorporation in the silica matrix. The interatomic distances of both shells are the same as in the $Zr_4O_2(OMc)_{12}$ cluster. For the ZS40.0_as prepared sample a similar investigation could not be done due to the bad quality of the spectrum. The high noise made an EXAFS analysis impossible.

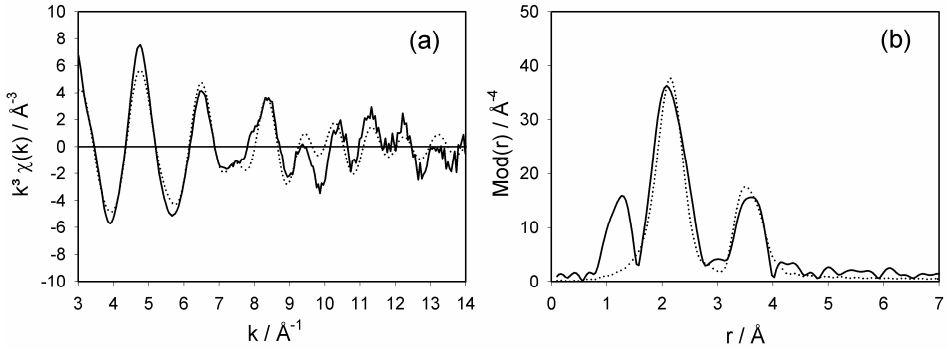


**Fig. 2.16:** Experimental (solid line) and simulated (dotted line) EXAFS functions and their corresponding Fourier transforms for the ZS1.3_as prepared sample.

**Table 2.3:** Structural parameters for the $Zr_4O_2(OMc)_{12}$ (fitting 1 and 2) and the ZS1.3_as prepared sample.

| | A-Bs[a] | N[b] | r[c] [Å] | σ[d] [Å] | $E_f$ [e] [eV] | k-range [$Å^{-1}$] | Fit Index |
|---|---|---|---|---|---|---|---|
| **$Zr_4O_2(OMc)_{12}$** (fitting 1) | Zr – O<br>Zr – Zr<br>Zr – Zr | 7.5<br>0.5<br>2 | 2.20<br>3.33<br>3.51 | 0.095<br>0.050<br>0.063 | 6.56 | 3– 14 | 32.08 |
| **$Zr_4O_2(OMc)_{12}$** (fitting 2) | Zr – O<br>Zr –Zr | 7.5<br>2.0 | 2.20<br>3.52 | 0.097<br>0.071 | 6.53 | 3– 14 | 32.50 |
| **ZS1.3_as prepared** | Zr – O<br>Zr – Zr | 7.5<br>2.0 | 2.20<br>3.53 | 0.107<br>0.084 | 6.92 | 3– 14 | 36.80 |
| **XRD $Zr_4O_2(OMc)_{12}$** | Zr– O<br>Zr –Zr<br>Zr –Zr | 7.5<br>0.5<br>2.0 | 2.18<br>3.30<br>3.67 | | | | |

[a] absorber (A) – backscatterers (Bs), [b] coordination number N, [c] interatomic distance r, [d] Debye-Waller factor σ and [e] edge position (Fermi energy) relative to calculated vacuum zero $E_f$

## 2.6 Effect of the temperature

In order to study the influence of the temperature on the local structure, samples with two different Si/Zr molar ratios namely 1.3 : 1 and 40.0 : 1, annealed at 500°C, 700°C, 900°C, 1000°C were analysed.

### 2.6.1 XANES of the samples with a Si/Zr molar ratio of 1.3

In figure 2.17 the XANES spectra of the different samples are compared. For a better overview, the derivatives of the XANES spectra of these samples are depicted in figure 2.18.

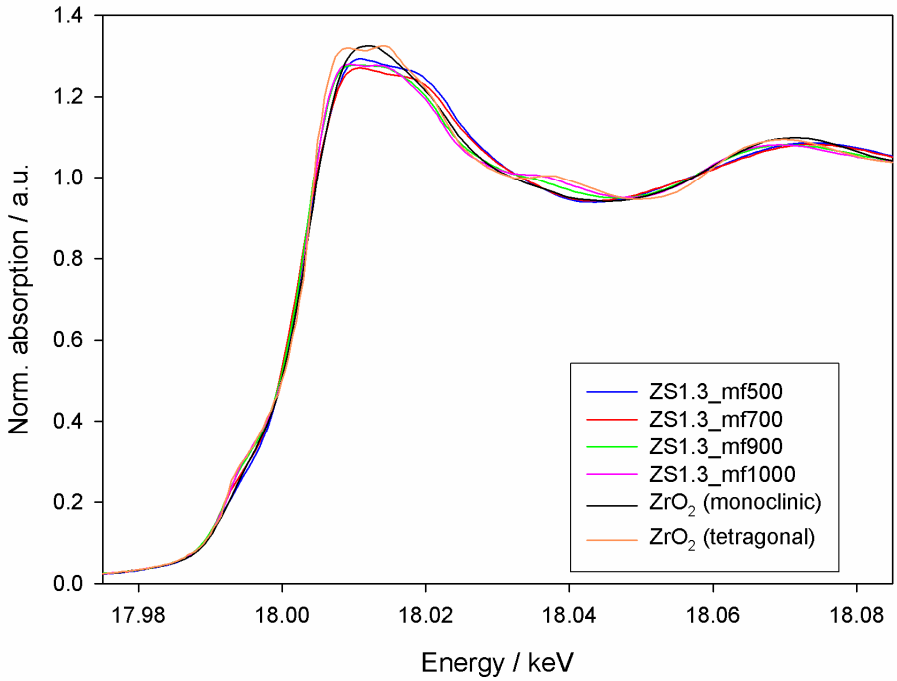


**Figure 2.17:** XANES spectra of the samples with a Si/Zr ratio of 1.3.

The edge width (see first derivative) for the two samples annealed at high temperatures (ZS1.3_mf900 and ZS1.3_mf1000) is very similar.

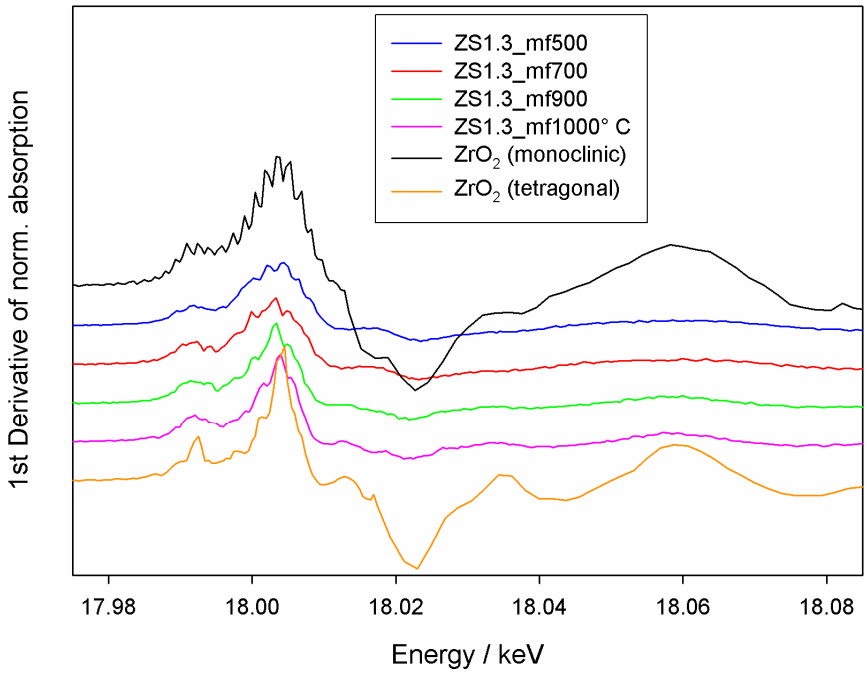


**Figure 2.18:** First derivatives of the XANES spectra of the samples with a Si/Zr ratio of 1.3.

For the two samples annealed at lower temperature, i.e. 500 and 700°C, the edge width is broader and the shoulder at 18.037 keV is not observed and the pre-peak at 17.993 keV-typical has a much smaller intensity.

In contrast to the two high temperature samples the white line of samples ZS1.3_mf500 and ZS1.3_mf700 exhibits a plateau-like shape with a negative slope. In literature [G. Mountjoy *et al.* (2000)] it is described that the slope of the white line for zirconia-silica xerogels (as unheated and heated at 750°C) is strongly dependent on the Si/Zr molar ratio. Samples with a Si/Zr molar ratio higher than 4.0 are reported to have a positive slope whereas samples with smaller ratios show a negative slope. This can be explained by the fact that low temperature samples are more disordered.

### 2.6.2 EXAFS of the samples with a Si/Zr molar ratio of 1.3

The fitting of the experimental data was carried out according to the results of the XANES evaluation. For the ZS1.3_mf500 sample a three shell model with two O-shells and one Zr-shell was fitted. The experimentally determined and theoretically simulated EXAFS functions of the samples and their Fourier transforms are shown in figure 2.19. Here it can be seen that the oxygen peaks of

the two low temperature samples are broader than the peaks of the high temperature samples, which implies disordered structure. Furthermore, they exhibit a shoulder on the right side of the oxygen peak according to the more disordered oxygen coordination of the Zr atom in the low temperature samples. The structural parameters determined by EXAFS are presented in table 2.4.

The same approach discussed for the sample annealed 500°C was also used for the ZS1.3_mf700 sample. As far as the ZS1.3_mf700 sample is concerned, the results are very similar. Only the coordination number of the Zr-shell increased to 2.7 whereas sample ZS1.3_mf500 showed a coordination number of 2. This difference is a result of the different annealing temperature of 500°C and 700°C. With increasing temperature, the phase separated $ZrO_2$ domains can grow in size and become more crystalline due to further condensation and to the removal of remaining organic moieties. Accordingly, an increase in the Zr-Zr coordination number from 2 (ZS1.3_mf500) to 4 (ZS1.3_mf1000) was observed (see table 2.4).

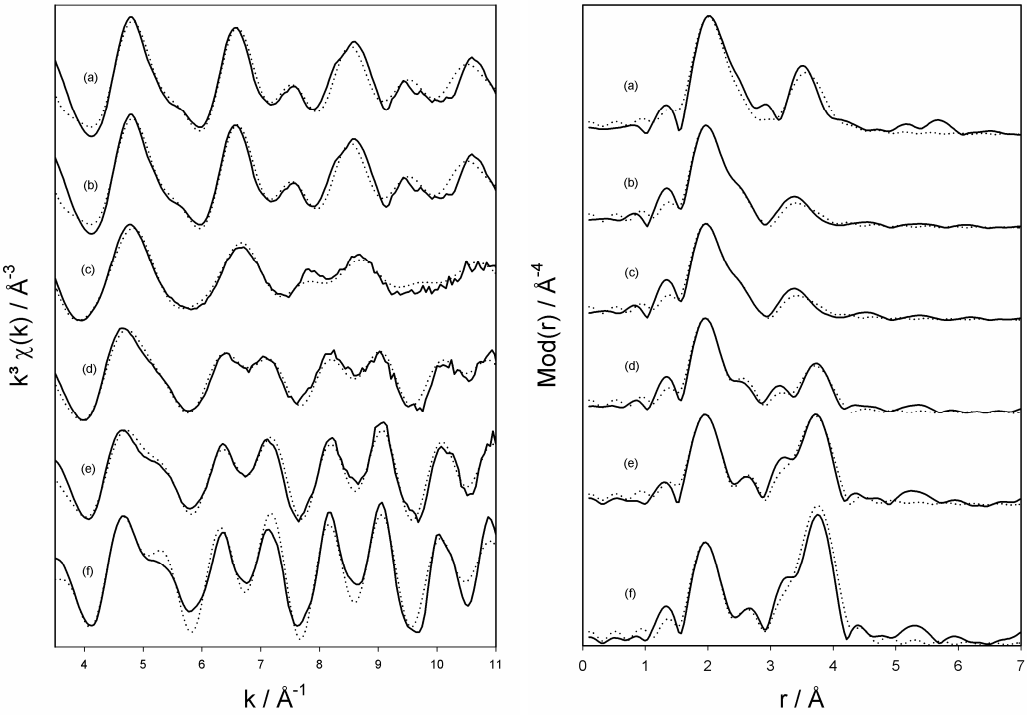


**Figure 2.19:** Experimental (solid line) and simulated (dotted line) EXAFS functions and their corresponding Fourier transforms for the samples: **(a)** monoclinic $ZrO_2$, **(b)** ZS1.3_mf500, **(c)** ZS1.3_mf700, **(d)** ZS1.3_mf900, **(e)** ZS1.3_mf1000, **(f)** tetragonal $ZrO_2$.

For the remaining samples annealed at higher temperatures, different considerations have been made.

Accordingly, for ZS1.3_mf900 two O-shells and one Zr-shell could be fitted at the distances 2.11 Å, 2.31 Å and 3.63 Å (table 2.4). Interestingly, the coordination number of the Zr-shell with the value of 2.3 is smaller than 2.7 for sample ZS1.3_mf700 at a lower temperature. This can be explained by a rearrangement of the local structure from a more disordered one to a more ordered one. Nevertheless, it should be mentioned that the difference of the Zr-shell is within the error bar for the coordination number. The change from a short-range order to a low-range one is outined by the XRD measurements which show the typical reflexes of tetragonal $ZrO_2$ (figure 2.20) for samples annealed at higher temperature.

The sample ZS1.3_mf1000 was investigated with the same approach already described for ZS1.3_mf900. The sample ZS1.3_mf1000 shows a high crystallinity (XRD) and its peaks are much sharper than for sample ZS1.3_mf900.

**Table 2.4:** Structural parameters for the samples: **(a)** monoclinic $ZrO_2$, **(b)** ZS1.3_mf500, **(c)** ZS1.3_mf700, **(d)** ZS1.3_mf900, **(e)** ZS1.3_mf1000 samples, **(f)** tetragonal $ZrO_2$.

| | A-Bs[a] | N[b] | r[c] [Å] | σ[d] [Å] | $E_f$ [e] [eV] | k-range [$Å^{-1}$] | Fit Index |
|---|---|---|---|---|---|---|---|
| $ZrO_2$(monoclinic) | Zr – O<br>Zr – O<br>Zr – Zr | 3.0<br>4.0<br>7.0 | 2.08<br>2.23<br>3.48 | 0.050<br>0.074<br>0.120 | 7.23 | 3.5– 11 | 28.18 |
| ZS1.3_mf500 | Zr – O<br>Zr – O<br>Zr – Zr | 3.0<br>4.0<br>2.0 | 2.10<br>2.27<br>3.41 | 0.050<br>0.077<br>0.112 | 3.14 | 3.5– 11 | 20.61 |
| ZS1.3_mf700 | Zr – O<br>Zr – O<br>Zr – Zr | 3.0<br>4.0<br>2.7 | 2.09<br>2.26<br>3.41 | 0.055<br>0.081<br>0.122 | 3.35 | 3.5– 11 | 23.67 |
| ZS1.3_mf900 | Zr – O<br>Zr – O<br>Zr – Zr | 4.0<br>4.0<br>2.3 | 2.11<br>2.31<br>3.63 | 0.071<br>0.092<br>0.087 | 2.83 | 3.5– 11 | 24.46 |
| ZS1.3_mf1000 | Zr – O<br>Zr – O<br>Zr – Zr | 4.0<br>4.0<br>4.0 | 2.10<br>2.31<br>3.63 | 0.074<br>0.107<br>0.081 | 4.47 | 3.5– 11 | 26.08 |
| $ZrO_2$(tetragonal) | Zr – O<br>Zr – O<br>Zr – Zr | 4.0<br>4.0<br>12.0 | 2.10<br>2.30<br>3.63 | 0.067<br>0.097<br>0.107 | 5.81 | 3.5– 11 | 31.16 |

[a] absorber (A) – backscatterers (Bs), [b] coordination number N, [c] interatomic distance r, [d] Debye-Waller factor σ and [e] edge position (Fermi energy) relative to calculated vacuum zero $E_f$

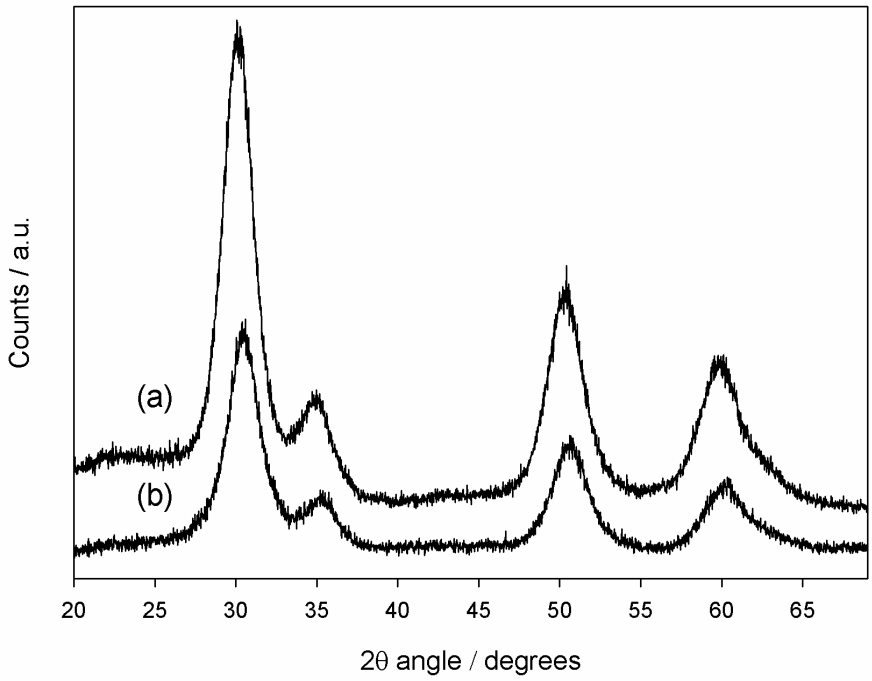


**Figure 2.20:** XRD diffractogramms for samples: **(a)** ZS1.3_mf1000, **(b)** ZS1.3_mf900.

### 2.6.3 XANES of the samples with a Si/Zr molar ratio of 40.0

In figure 2.21 the XANES spectra of the samples with a Si/Zr ratio of 40.0 are depicted. At the first glance, the spectra show the same characteristic behaviour only with small deviations. In particular, a broad, plateau-shaped white line with a positive slope can be observed. Due to the resemblance of this XANES spectrum to the spectra of $Zr(OPr^n)_4$ (figure 2.23) and $BaZrO_3$ and $Na_2ZrSi_3O_9 \cdot 2H_2O$ (catapleiite) [Mountjoy, G. *et al.* (2000), Mountjoy, G. *et al.* (2003), Turrillas, X. *et al*. (1993), Farges, F. e*t al*. (1991)] a structure containing $ZrO_6$ polyhedra could be assumed. However, the EXAFS analysis indicates a disordered local environment and an overall O-coordination of about 8 for the samples. For the reason of completeness, figure 2.22 shows the first derivatives of the XANES spectra of the samples with a Si/Zr molar ratio of 40.0.

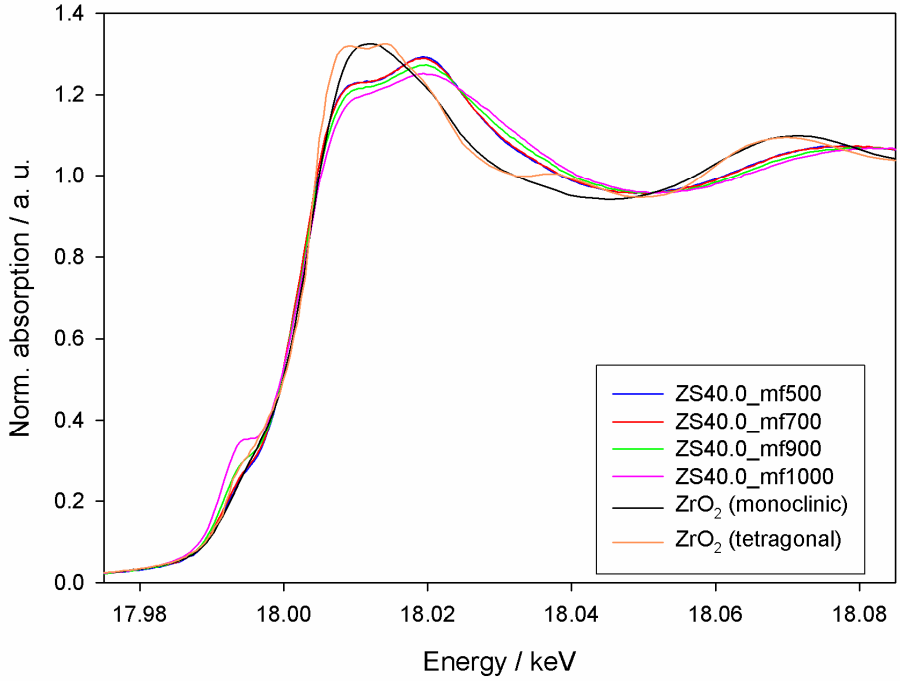


**Figure 2.21:** XANES spectra of the samples with a Si/Zr molar ratio of 40.0.

In summary, the formation of a completely amorphous structure can be assumed. This is also in accordance with the very low Zr-Zr coordination number evidenced (≈ 1.2) which can be in turn related to the small amount of zirconium atoms incorporated in the silica matrix.

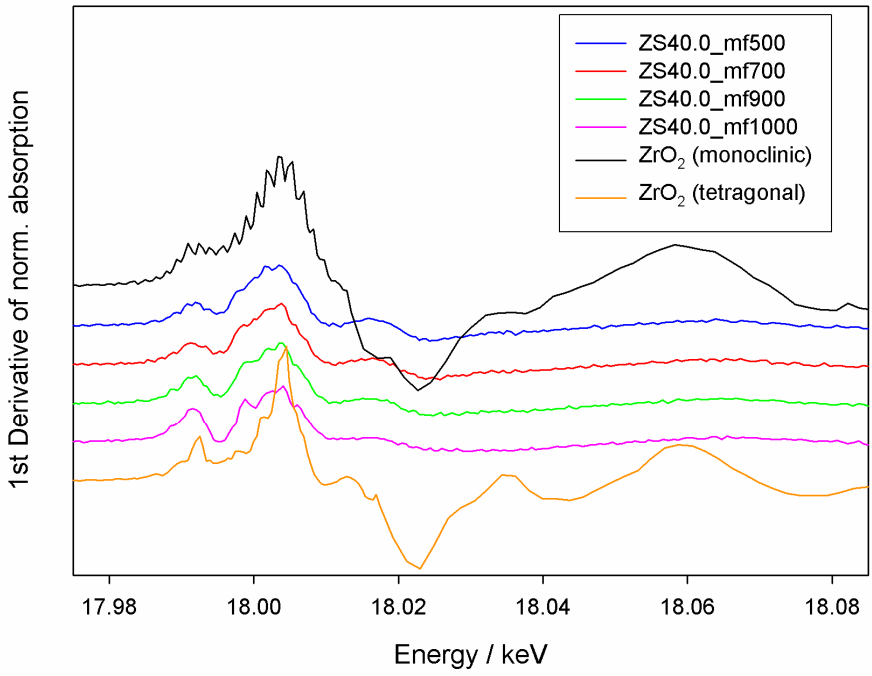


**Figure 2.22:** First derivatives of the XANES spectra of the samples with a Si/Zr molar ratio of 40.0.

### 2.6.4 EXAFS of the samples with a Si/Zr molar ratio of 40.0

According to the analysis of the samples with a Si/Zr molar ratio of 1.3, a three shell model with two O-shells and one Zr-shell was fitted. The experimentally determined and theoretically simulated EXAFS functions and their Fourier transforms are shown in the figure 2.24. The determined structural parameters by EXAFS are presented in the table 2.5. The combined O-coordination of the first two shells is about 8. As already mentioned in the XANES discussion, a small amount of the Zr-atoms could be coordinated by 6 oxygen atoms. Further evidence for the formation of $ZrO_6$ polyhedra is given by the short distance of the first Zr-O shell with a value of 2.03 Å. This is about 0.07 Å shorter than in the higher concentrated (Si/Zr = 1.3) samples. Typical Zr-O distances for 6-coordinated Zr are in the range of 2.03 Å to 2.11 Å [Farges, F. *et al.* (1991)]. EXAFS results show a coordination number of about 1 for the Zr-shell. The corresponding Zr-Zr distance is 3.33 Å. A coordination number of 1 can also be found in Zr n-propoxide (figure 2.23). Here, the structure is characterised by a 6-fold oxygen coordination comprising of Zr-O-R, Zr-$(OR)_2$-Zr and Zr-(ROH) elements. For these samples EXAFS analysis indicates a similar dimeric structure with R being replaced by Si– and H– atoms. However for samples ZS40.0_mf900 and ZS40.0_mf1000 a distorted octahedral coordination with an additional, weakly bound O-ligand could be assumed. Such additional ligands (e.g. water) have been proposed for Zr in Zr hydroxide [Mountjoy, G. et al. (2000), Turrillas, X. *et al.* (1993)].

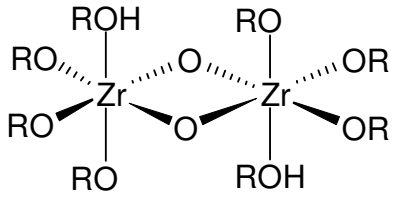


**Figure 2.23:** The structure of Zr-n-propoxide

In fact, the dilution of Zr in the silica matrix accounts for the difficult formation of $ZrO_2$ low range ordered systems. XRD spectra of these samples are actually characterised by amorphous patterns (data not reported).

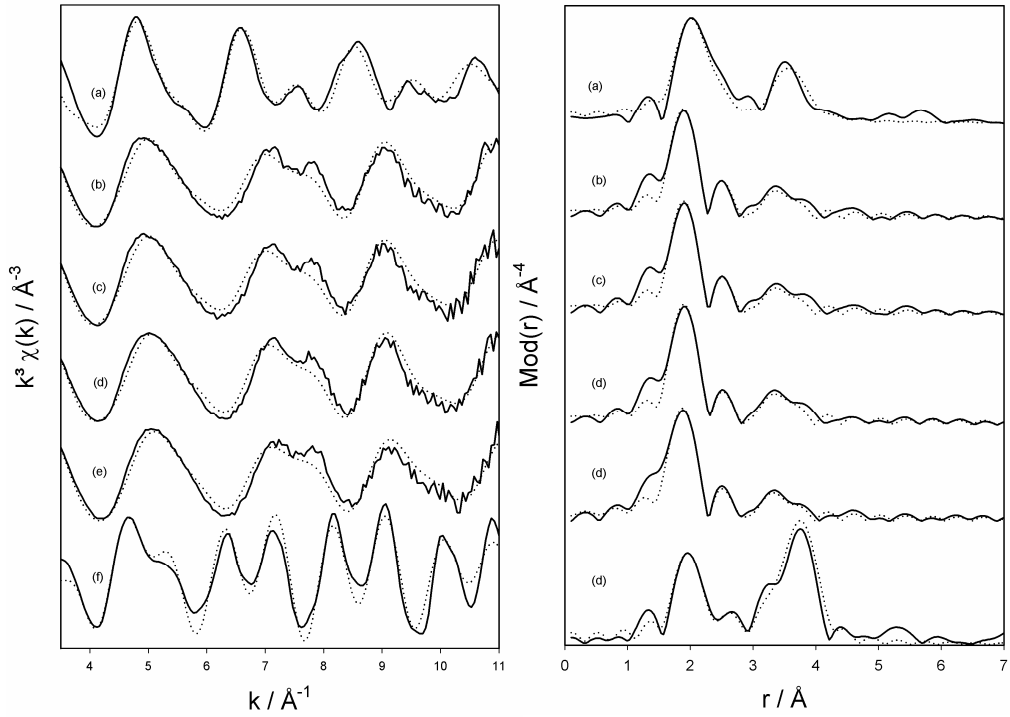


**Fig. 2.24:** Experimental (solid line) and simulated (dotted line) EXAFS functions and their corresponding Fourier transforms for the samples: **(a)** monoclinic $ZrO_2$, **(b)** ZS40.0_mf500, **(c)** ZS40.0_mf700, **(d)** ZS40.0_mf900 **(e)** ZS40.0_mf1000 samples, **(f)** tetragonal $ZrO_2$.

**Table 2.5:** Structural parameters for the samples: **(a)** monoclinic $ZrO_2$, **(b)** ZS40.0_mf500, **(c)** ZS40.0_mf700, **(d)** ZS40.0_mf900, **(e)** ZS40.0_mf1000 samples, **(f)** tetragonal $ZrO_2$.

| | A-Bs[a] | N[b] | r[c] [Å] | σ[d] [Å] | $E_f$ [e] [eV] | k-range [$Å^{-1}$] | Fit Index |
|---|---|---|---|---|---|---|---|
| $ZrO_2$(monoclinic) | Zr – O | 3.0 | 2.08 | 0.050 | 7.23 | 3.5– 11 | 28.18 |
| | Zr – O | 4.0 | 2.23 | 0.074 | | | |
| | Zr – Zr | 7.0 | 3.48 | 0.120 | | | |
| ZS40.0_mf500 | Zr – O | 4.0 | 2.03 | 0.055 | 4.62 | 3.5– 11 | 25.94 |
| | Zr – O | 4.1 | 2.26 | 0.092 | | | |
| | Zr – Zr | 1.1 | 3.33 | 0.084 | | | |
| ZS40.0_mf700 | Zr – O | 4.1 | 2.03 | 0.055 | 4.60 | 3.5– 11 | 28.53 |
| | Zr – O | 4.2 | 2.26 | 0.097 | | | |
| | Zr – Zr | 1.2 | 3.33 | 0.089 | | | |
| ZS40.0_mf900 | Zr – O | 4.1 | 2.02 | 0.055 | 4.71 | 3.5– 11 | 26.44 |
| | Zr – O | 4.2 | 2.25 | 0.107 | | | |
| | Zr – Zr | 1.2 | 3.32 | 0.084 | | | |
| ZS40.0_mf1000 | Zr – O | 4.0 | 2.00 | 0.059 | 5.78 | 3.5– 11 | 28.98 |
| | Zr – O | 4.2 | 2.22 | 0.110 | | | |
| | Zr – Zr | 1.0 | 3.31 | 0.084 | | | |
| $ZrO_2$(tetragonal) | Zr – O | 4.0 | 2.10 | 0.067 | 5.81 | 3.5– 11 | 31.16 |
| | Zr – O | 4.0 | 2.30 | 0.097 | | | |
| | Zr – Zr | 12.0 | 3.63 | 0.107 | | | |

[a] absorber (A) – backscatterers (Bs), [b] coordination number N, [c] interatomic distance r, [d] Debye-Waller factor σ and [e] edge position (Fermi energy) relative to calculated vacuum zero $E_f$

## 2.7 Effect of the composition

In order to determine the influence of the composition on the local structure, samples with different Si/Zr ratio were systematically investigated. To this aim, six samples characterised by Si/Zr molar ratios ranging from 1.3 : 1 to 40.0 : 1 were all annealed at 1000°C and investigated by means of EXAFS spectroscopy.

### 2.7.1 XANES of the samples annealed at 1000°C

The XANES spectra of the figure 2.25 suggest that, at high concentration, a local environment similar to that of tetragonal $ZrO_2$ is present. In fact, the five most concentrated samples (Si/Zr ratio of 1.3, 2.5, 5.0, 10.0, and 20.0) show features similar to the tetragonal $ZrO_2$ reference such as the twin peak feature of the white line and the shoulder at 18.037 keV. Nevertheless, it should be pointed out that the intensity of these features is progressively reduced with decreasing Zr concentration. The double peak is less pronounced than in the tetragonal reference, reaching a plateau with a slope of zero for the less concentrated samples (ZS10.0_mf1000 and ZS20.0_mf1000). This behaviour is typical for small domains of $ZrO_2$ in a matrix. As the XANES region is strongly influenced by multiple scattering, the increased disorder of particles with limited size smears out sharp signals [Farges, F. *et al.* (1997)].

It should be noted that for the ZS10.0_mf1000 and ZS20.0_mf1000 samples the shoulder at 18.037 keV is not as pronounced as in pure tetragonal zirconia but the spectrum exhibits an increased absorption in the same region similar to a tetragonal local structure. The samples with a higher Zr-content such as ZS5.0_mf1000, ZS2.5_mf1000 and ZS1.3_mf1000 show a very pronounced shoulder at 18.037 keV. Additionally, the double peak feature of the white line and the pre-peak at 17.993 keV support the formation of a structure similar to tetragonal $ZrO_2$. Especially for the two highest concentrated samples, the tetragonal nature of the structure can also be seen in the first derivative of the XANES spectra (figure 2.26). Accordingly, the XRD patterns of the sample with Si/Zr ratios of 1.3, 2.5, 5.0 and 10.0 show the typical reflexes of tetragonal $ZrO_2$

(figure 2.27). For sample ZS20.0_mf1000 the peaks are very broad, which indicates that the tetragonal domains are small and disordered. Sample ZS40.0_mf1000 is completely amorphous.

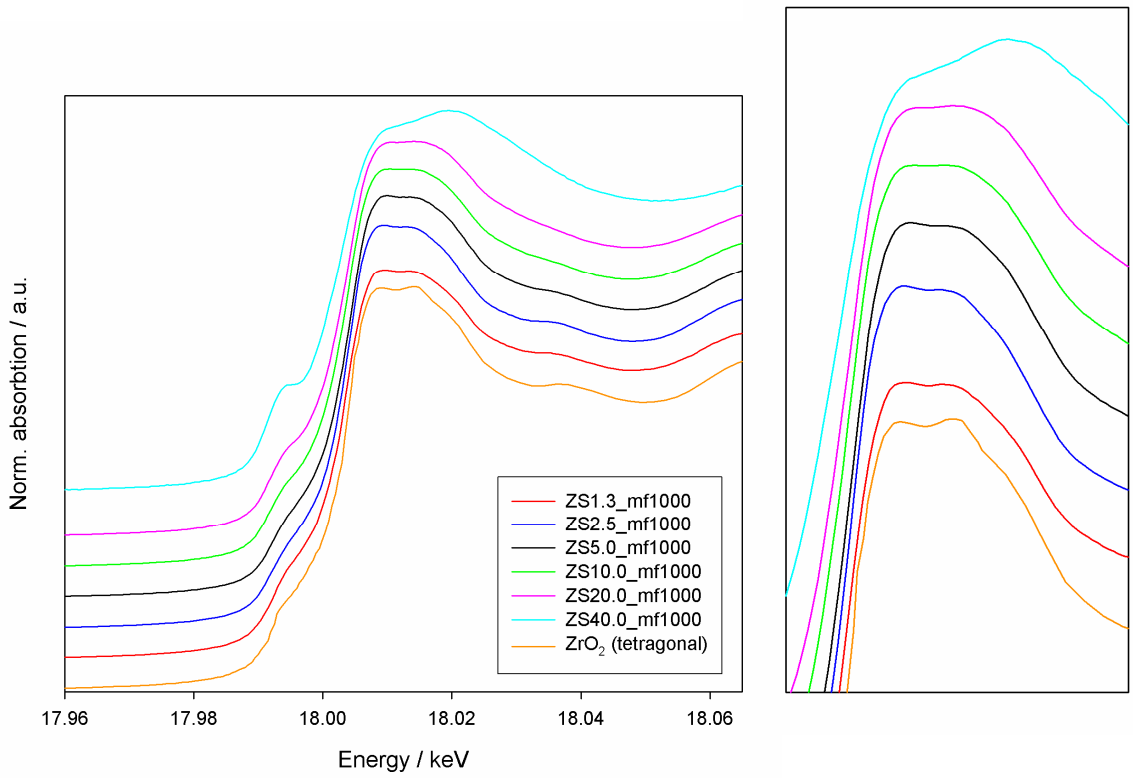


**Figure 2.25:** Shifted XANES spectra of the samples annealed at 1000° C.

The more diluted sample (ZS40.0_mf1000) is instead characterised by a broad, plateau-shaped white line with a positive slope. Interestingly, the pre-edge peak at 17.993 keV is present in all samples but with a greater intensity in the less concentrated ones (ZS40.0_mf1000 and ZS20.0_mf1000) than in the tetragonal reference. This can be attributed to a more disordered and less centrosymmetric Zr-O geometry due to the high dilution of the Zr-atoms inside the silica matrix.

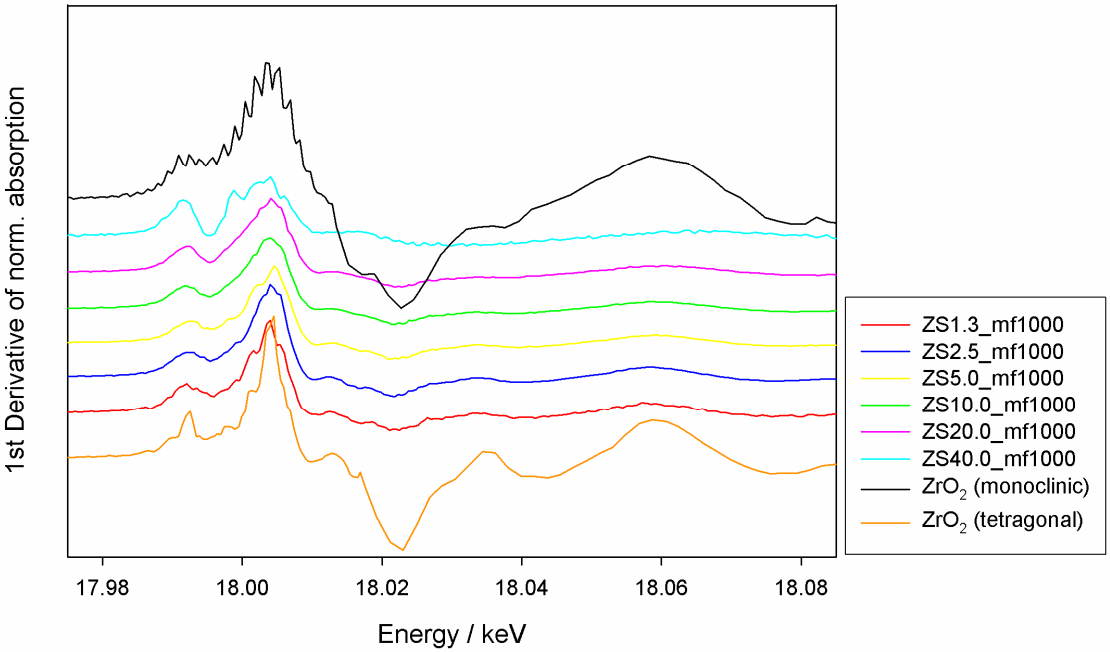


**Figure 2.26:** First derivatives of the XANES spectra of the samples with a different Si/Zr ratio annealed at 1000° C.

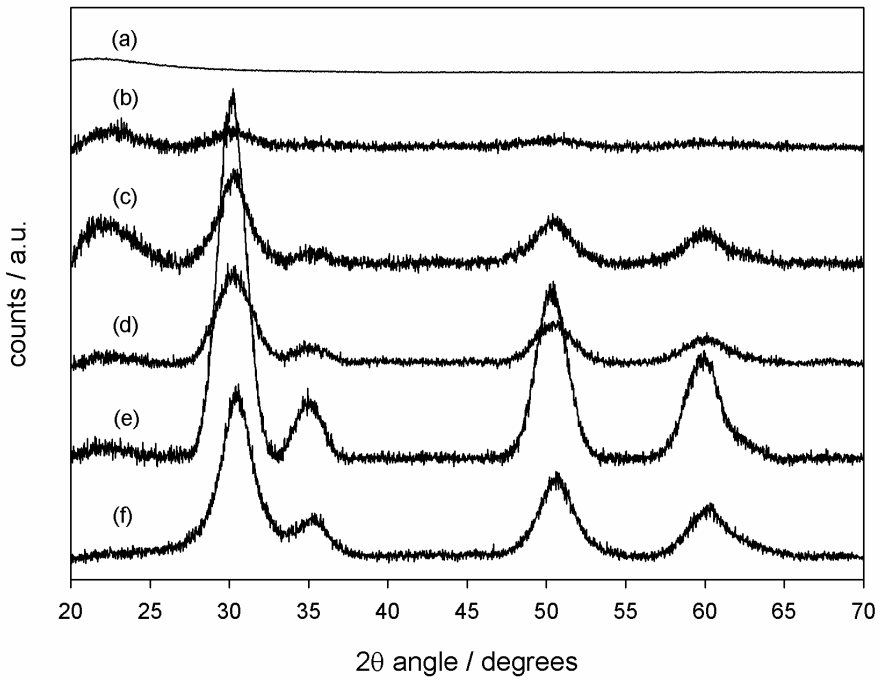


**Figure 2.27:** XRD diffractogramms for samples: **(a)** ZS40.0_mf1000, **(b)** ZS20.0_mf900, **(c)** ZS10.0_mf1000, **(d)** ZS5.0_mf1000, **(e)** ZS2.5_mf1000 and **(f)** ZS1.3_mf1000.

In summary, the typical features of tetragonal $ZrO_2$ are more pronounced as the Zr-concentration is increased (lower Si/Zr ratio). Consequently, there is a characteristic tendency for all the samples annealed at 1000°C to build up a structure similar to the tetragonal $ZrO_2$. Only the sample with the lowest Si/Zr ratio (ZS40.0_mf1000) shows different features. It seems appropriate to describe this sample with an amorphous structure model. Accordingly, both TEM and XRD analysis do not show for these samples any crystalline or aggregation feature (data are not reported).

### 2.7.2 EXAFS of the samples annealed at 1000°C

The experimental EXAFS data of the samples with different Si/Zr ratio was analysed taking the results of the XANES investigations into account. For all these samples, a three shell model with two O-shells and one Zr-shell similar to tetragonal $ZrO_2$ was fitted. The coordination numbers of the first two shells were fixed to 4 in accordance with the tetragonal modification and coordination number of the Zr shell, the interatomic distances and the Debye-Waller factors were iterated. For sample ZS40.0_mf1000, an additional iteration was performed: the Debey-Waller factors of the first two shells were fixed and the other parameters were iterated. This leads to a coordination number of 4.2 for the second oxygen shell. The structural parameters determined by EXAFS are tabulated in the table 2.6. These parameters are identical to those obtained for tetragonal $ZrO_2$. Only slightly different distances for the two oxygen shells could be noted, but these differences are still within the error bars of coordination numbers.

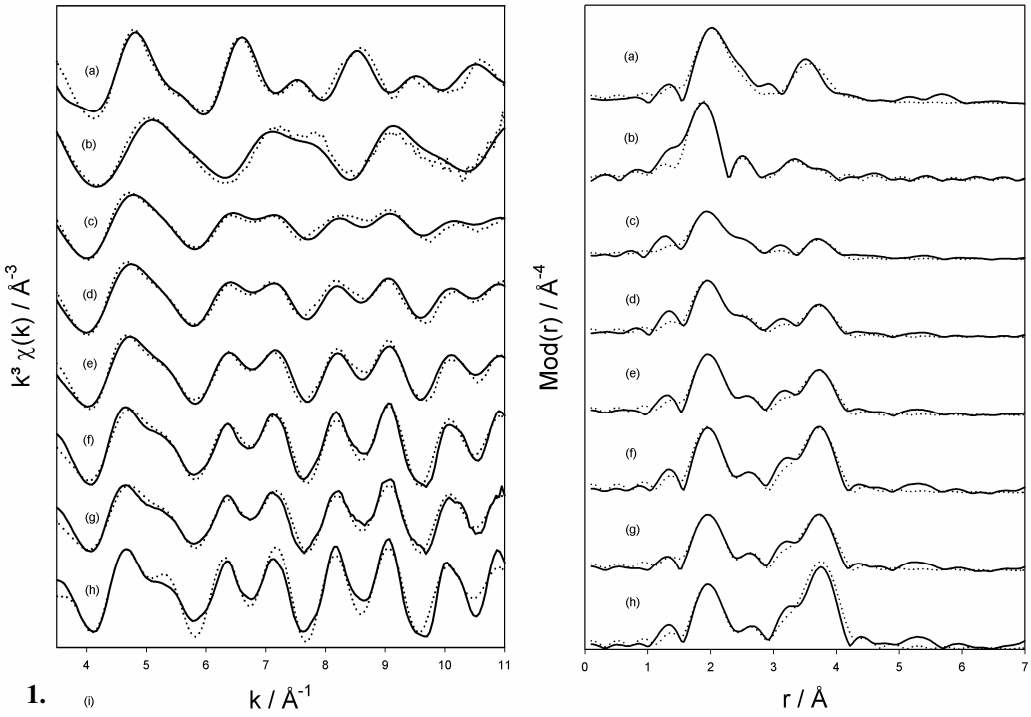


1. (i)

**Figure 2.28:** Experimental (solid line) and simulated (dotted line) EXAFS functions and their corresponding Fourier transforms for the samples: **(a)** monoclinic $ZrO_2$, **(b)** ZS40.0_mf1000, **(c)** ZS20.0_mf1000, **(d)** ZS10.0_mf1000, **(e)** ZS5.0_mf1000, **(f)** ZS2.5_mf1000, **(g)** ZS1.3_mf1000 samples, **(h)** tetragonal $ZrO_2$.

The distances determined for the sample ZS40.0_mf1000 are completely different from those of the other samples. In accordance with the lower amount of zirconium atoms incorporated in the silica matrix at a Si/Zr ratio of 40.0, the formation of an amorphous structure different from tetragonal zirconia can be assumed. Moreover, the two-fold doublet structure in the χ(k)-function (see chapter 2.2) characteristic of tetragonal $ZrO_2$, is more emphasised as the Zr-content is increased (figure 2.28). In the ZS40.0_mf1000 sample, this feature is completely missing (figure 2.28). The comparison of the Fourier transforms of the six samples leads to the same conclusions. The oxygen peak of the ZS40.0_mf1000 sample is broader and slightly higher than in the other samples. The question whether this result is only due to the formation of smaller $ZrO_2$ domains caused by higher dilution or if a completely different short range order is present can not be answered in this work.

In table 2.6, it can be clearly seen that an increase of the Zr concentration (lower Si/Zr ratio) leads to a higher coordination number of the Zr-shell. Only for sample ZS1.3_mf1000 this behaviour is not observed (but the difference is still within the error bar). The coordination number of the third shell is smaller than for the

sample with a smaller Zr-content. So, one could conclude that the $ZrO_2$ domains in sample ZS2.5_mf1000 are larger in size and less disordered. This could be attributed to the fact that sample ZS1.3_mf1000 was annealed for four hours in a tubular oven, where a strict control of the temperature is hardly achieved, whereas sample ZS2.5_mf1000 was annealed for five hours in a muffle oven, where the annealing is more efficient. This is also in agreement with the XRD spectra, which show an increasing crystallinity for higher Zr concentrations except for sample ZS1.3_mf1000.

These data are in agreement with XRD and TEM data. While the former show well defined and sharp reflexes (figure 2.27) for the more concentrated samples, amorphous patterns were instead detected for the more diluted ZS40.0_mf1000 and ZS20.0_mf1000 samples. Accordingly, TEM micrographs are completely featureless for sample ZS40.0_mf1000, whereas the presence of well distributed zirconia nanoparticles was evidenced for samples ZS2.5_mf1000 and ZS5.0_mf1000 (data not shown).

**Table 2.6:** Structural parameters for the samples: **(a)** monoclinic $ZrO_2$, **(b)** ZS40.0_mf1000, **(c)** ZS20.0_mf1000, **(d)** ZS10.0_mf1000, **(e)** ZS5.0_mf1000, **(f)** ZS2.5_mf1000 and **(g)** ZS1.3_mf1000, **(h)** tetragonal $ZrO_2$.

| | A-Bs[a] | N[b] | r[c] [Å] | σ[d] [Å] | $E_f$ [e] [eV] | k-range [$Å^{-1}$] | Fit Index |
|---|---|---|---|---|---|---|---|
| $ZrO_2$(monoclinic) | Zr – O<br>Zr – O<br>Zr – Zr | 3.0<br>4.0<br>7.0 | 2.08<br>2.23<br>3.48 | 0.050<br>0.074<br>0.120 | 7.23 | 3.5– 11 | 28.18 |
| ZS40.0_mf1000 | Zr – O<br>Zr – O<br>Zr – Zr | 4.0<br>4.2<br>1.0 | 2.00<br>2.22<br>3.31 | 0.059<br>0.110<br>0.084 | 5.78 | 3.5– 11 | 28.98 |
| ZS20.0_mf1000 | Zr – O<br>Zr – O<br>Zr – Zr | 4.0<br>4.0<br>2.2 | 2.09<br>2.28<br>3.62 | 0.089<br>0.105<br>0.105 | 2.66 | 3.5– 11 | 29.31 |
| ZS10.0_mf1000 | Zr – O<br>Zr – O<br>Zr – Zr | 4.0<br>4.0<br>2.5 | 2.10<br>2.30<br>3.63 | 0.074<br>0.095<br>0.089 | 3.25 | 3.5– 11 | 25.52 |
| ZS5.0_mf1000 | Zr – O<br>Zr – O<br>Zr – Zr | 4.0<br>4.0<br>3.9 | 2.10<br>2.30<br>3.62 | 0.071<br>0.100<br>0.092 | 3.51 | 3.5– 11 | 23.05 |
| ZS2.5_mf1000 | Zr – O<br>Zr – O<br>Zr – Zr | 4.0<br>4.0<br>4.4 | 2.10<br>2.30<br>3.63 | 0.063<br>0.095<br>0.081 | 4.80 | 3.5– 11 | 23.92 |
| ZS1.3_mf1000 | Zr – O<br>Zr – O<br>Zr – Zr | 4.0<br>4.0<br>4.0 | 2.10<br>2.31<br>3.63 | 0.074<br>0.107<br>0.081 | 4.47 | 3.5– 11 | 26.08 |
| $ZrO_2$(tetragonal) | Zr – O<br>Zr – O<br>Zr – Zr | 4.0<br>4.0<br>12.0 | 2.10<br>2.30<br>3.63 | 0.067<br>0.097<br>0.107 | 5.81 | 3.5– 11 | 31.16 |

[a] absorber (A) – backscatterers (Bs), [b] coordination number N, [c] interatomic distance r, [d] Debye-Waller factor σ and [e] edge position (Fermi energy) relative to calculated vacuum zero $E_f$

### 2.7.3 XANES of the samples annealed at lower temperatures

The XANES spectra of the two sequences of samples (500°C/600°C and 700°C/800°C) at lower temperatures (figure 2.29) are very similar. The samples with the same composition, annealed at different temperatures, show nearly identical spectra. In fact, for a high concentration (low Si/Zr ratio) both spectra exhibit a negative slope whereas at low concentration a positive slope is observed. Both series do not show any well defined features of known species. The pre-edge peak at 17.993 keV is present in all samples, but with a low intensity. On the other hand, the edge width of the four samples with a higher Zr-content (ZS1.3_mf500, ZS5.0_mf600, ZS1.3_mf700 and ZS5.0_mf800) is broader and

similar (figure 2.29). Furthermore, the shoulder at 18.037 keV is not observed and the pre-peak at 17.993 keV is much less pronounced.

In contrast to the four samples at lower concentration (high Si/Zr ratio) the white line of the samples ZS1.3_mf500, ZS5.0_mf600, ZS1.3_mf700 and ZS5.0_mf800 shows a plateau-like shape with a negative slope (chapter 2.4.1 in literature [G. Mountjoy *et al.* (2000)]).

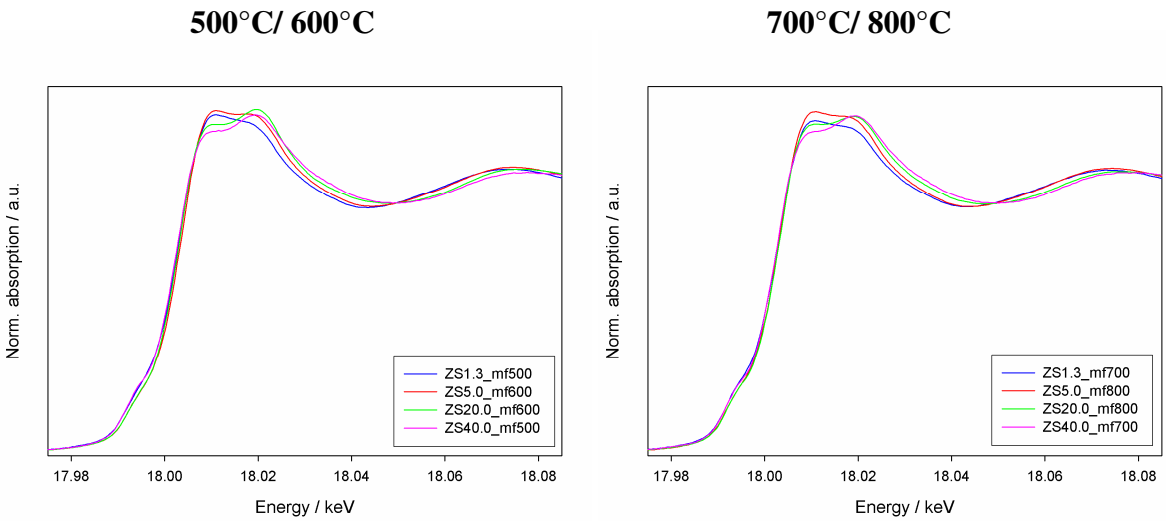


**Figure 2.29:** XANES spectra of the two sequences of samples annealed at 500°C/600°C and 700°C/800°C.

These results indicate that the local environment of samples with a high Zr content (low Si/Zr ratio) is similar to that of the monoclinic polymorph rather than the tetragonal one, whereas the formation of an amorphous structure different from monoclinic and tetragonal zirconia is assumed for the four samples with a lower Zr concentration (high Si/Zr ratio). This is also in accordance with the low annealing temperature. It should be noted that the annealing temperatures of the samples composed in figure 2.29 and 2.30 differ by 100°C (500°C /600°C for the first series and 700°C/800°C for the second series).

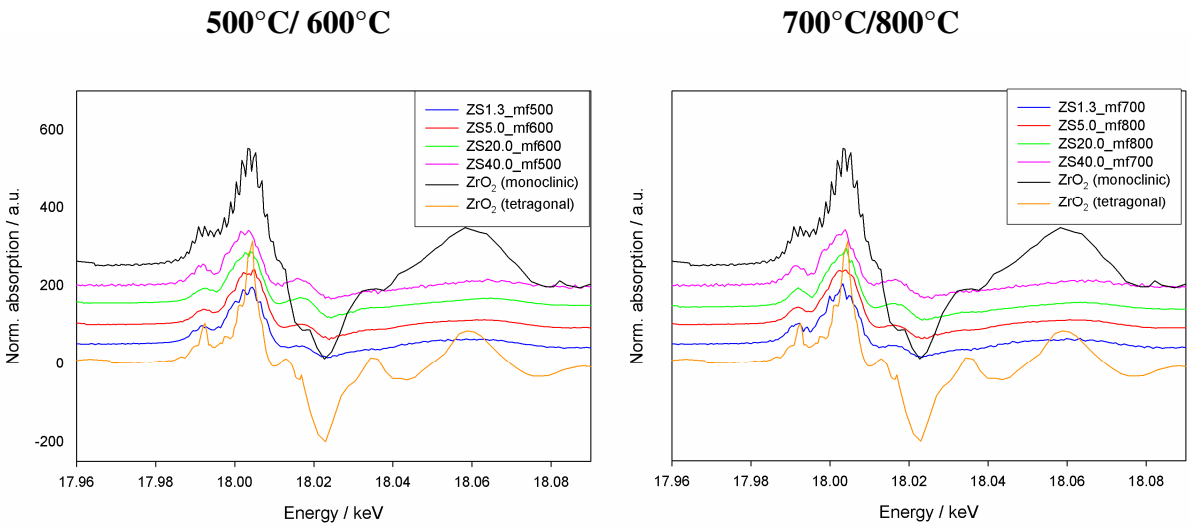


**Figure 2.30:** First derivative of the XANES spectra of the two sequences of samples with annealed at 500°C/600°C and 700°C/800°C.

### 2.7.4 EXAFS of the samples at lower temperatures

The fitting of the experimental data was carried out taking the results of the XANES data evaluation into account (chapter 2.7.3). In fact, for the high concentrated samples (ZS1.3_mf500, ZS5.0_mf600, ZS1.3_mf700 and ZS5.0_mf800), a three shell model with two O-shells and one Zr-shell was fitted. The structural parameters determined by EXAFS are listed in table 2.7 and 2.8.

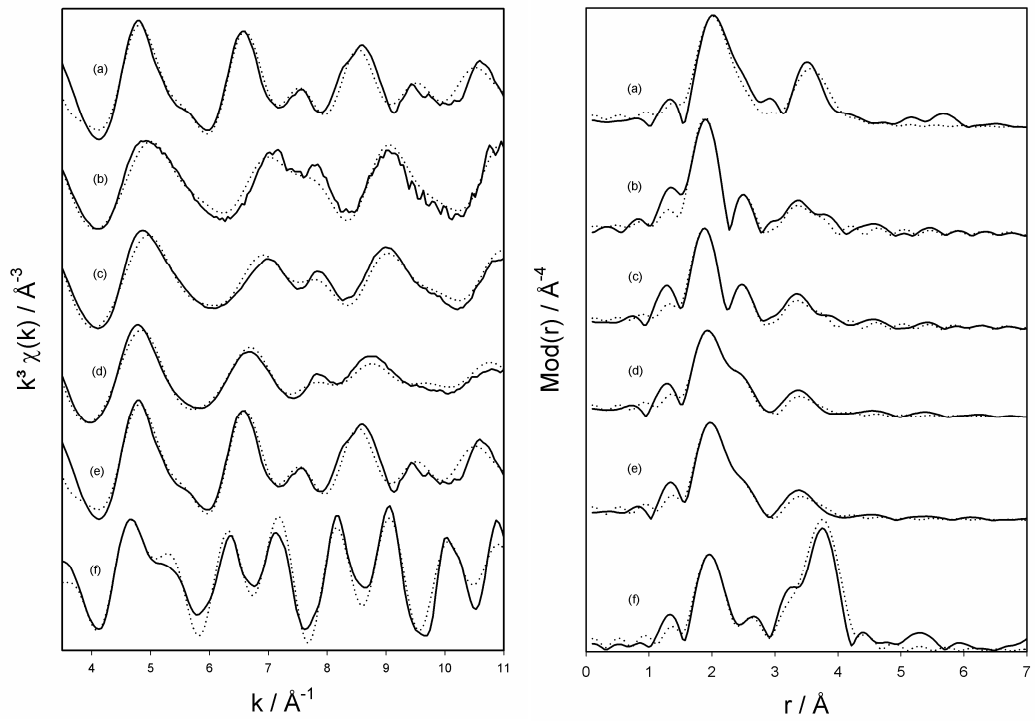


**Figure 2.31:** Experimental (solid line) and simulated (dotted line) EXAFS functions and their corresponding Fourier transforms for the samples: **(a)** monoclinic $ZrO_2$, **(b)** ZS40.0_mf500, **(c)** ZS20.0_mf600, **(d)** ZS5.0_mf600, **(e)** ZS1.3_mf500, **(f)** tetragonal $ZrO_2$.

The interatomic distances and the Debye-Waller factors of the two O-shells are almost identical for the four high concentrated samples. Only the coordination number of the Zr-shell of the sample ZS1.3_mf700 has increased to 2.7 whereas the others three samples exhibit a coordination number of about 2. This increase in coordination number of zirconium backscatter atom with increasing concentration is a general trend which has been already observed in the other analysed series (chapter 2.7.2). The different annealing temperatures of 500°C for sample ZS1.3_mf500 and 700°C for sample ZS1.3_mf700 can explain this behaviour. As already mentioned in chapter 2.6.2, with increasing temperature the phase separated $ZrO_2$ domains can grow in size and become less disordered due to further condensation and the removal of remaining organic moieties. Obviously, this effect is not observed for the sample ZS5.0_mf600 and ZS5.0_mf800. However, after calcinations at 1000°C (table 2.6) the coordination number of the Zr-shell is increased to 3.9.

**Table 2.7:** Structural parameters for the samples: **(a)** monoclinic $ZrO_2$, and **(b)** ZS40.0_mf500, **(c)** ZS20.0_mf600, **(d)** ZS5.0_mf600, **(e)** ZS1.3_mf500 samples, **(f)** tetragonal $ZrO_2$.

| | A-Bs[a] | N[b] | r[c] [Å] | σ[d] [Å] | $E_f$ [e] [eV] | k-range [$Å^{-1}$] | Fit Index |
|---|---|---|---|---|---|---|---|
| $ZrO_2$(monoclinic) | Zr – O | 3.0 | 2.08 | 0.050 | 7.23 | 3.5– 11 | 28.18 |
| | Zr – O | 4.0 | 2.23 | 0.074 | | | |
| | Zr – Zr | 7.0 | 3.48 | 0.120 | | | |
| ZS40.0_mf500 | Zr – O | 4.0 | 2.03 | 0.055 | 4.62 | 3.5– 11 | 25.94 |
| | Zr – O | 4.1 | 2.26 | 0.092 | | | |
| | Zr – Zr | 1.1 | 3.33 | 0.084 | | | |
| ZS20.0_mf600 | Zr – O | 4.0 | 2.04 | 0.063 | 3.88 | 3.5– 11 | 25.83 |
| | Zr – O | 4.0 | 2.25 | 0.081 | | | |
| | Zr – Zr | 1.4 | 3.34 | 0.095 | | | |
| ZS5.0_mf600 | Zr – O | 3.0 | 2.08 | 0.059 | 3.52 | 3.5– 11 | 24.33 |
| | Zr – O | 4.0 | 2.26 | 0.081 | | | |
| | Zr – Zr | 1.8 | 3.40 | 0.116 | | | |
| ZS1.3_mf500 | Zr – O | 3.0 | 2.10 | 0.050 | 3.14 | 3.5– 11 | 20.61 |
| | Zr – O | 4.0 | 2.27 | 0.077 | | | |
| | Zr – Zr | 2.0 | 3.41 | 0.112 | | | |
| $ZrO_2$(tetragonal) | Zr – O | 4.0 | 2.10 | 0.067 | 5.81 | 3.5– 11 | 31.16 |
| | Zr – O | 4.0 | 2.30 | 0.097 | | | |
| | Zr – Zr | 12.0 | 3.63 | 0.107 | | | |

[a] absorber (A) – backscatterers (Bs), [b] coordination number N, [c] interatomic distance r, [d] Debye-Waller factor σ and [e] edge position (Fermi energy) relative to calculated vacuum zero $E_f$

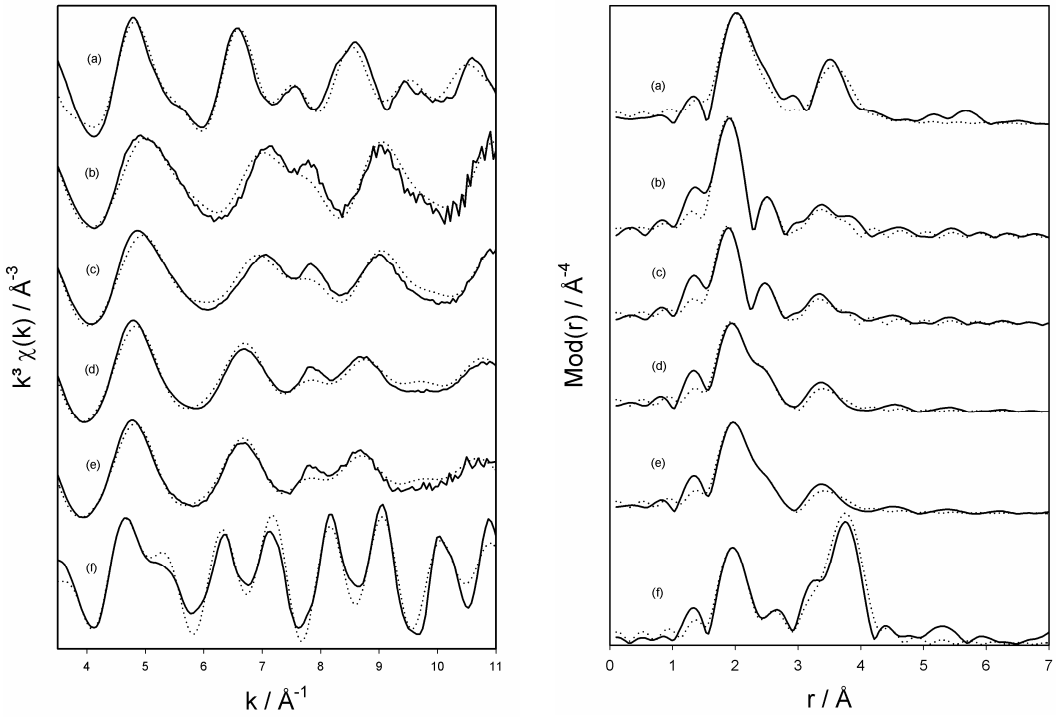


**Figure 2.32:** Experimental (solid line) and simulated (dotted line) EXAFS functions and their corresponding Fourier transforms for the samples: **(a)** monoclinic $ZrO_2$, **(b)** ZS40.0_mf700, **(c)** ZS20.0_mf800, **(d)** ZS5.0_mf800, **(e)** ZS1.3_mf700, **(f)** tetragonal $ZrO_2$.

For the samples with a lower Zr-content (ZS40.0_mf500, ZS20.0_mf600, ZS40.0_mf700 and ZS20.0_mf800), a three shell model with two O-shells and one Zr-shell was fitted. As the XANES spectra of the samples with a Si/Zr ratio of 20.0 are very similar to those of the samples with a Si/Zr ratio of 40.0, the same fit model was used. The structural parameters determined by EXAFS are presented in table 2.7 and 2.8. The combined O-coordination of the first two shells is about 8, but as already discussed in chapter 2.4.4 the short Zr-O distances of the first O-shell (2.04 Å, 2.03 Å) obtained by EXAFS analysis are also in agreement with a small contribution from $ZrO_6$ polyhedra. For all four samples, EXAFS results show a coordination number of about 1 for the Zr-shell.

**Table 2.8:** Structural parameters for the samples: **(a)** monoclinic $ZrO_2$, **(b)** ZS40.0_mf700, **(c)** ZS20.0_mf800, **(d)** ZS5.0_mf800 and **(e)** ZS1.3_mf700 samples, **(f)** tetragonal $ZrO_2$.

| | A-Bs[a] | N[b] | r[c] [Å] | σ[d] [Å] | $E_f$ [e] [eV] | k-range [$Å^{-1}$] | Fit Index |
|---|---|---|---|---|---|---|---|
| $ZrO_2$(monoclinic) | Zr – O<br>Zr – O<br>Zr – Zr | 3.0<br>4.0<br>7.0 | 2.08<br>2.23<br>3.48 | 0.050<br>0.074<br>0.120 | 7.23 | 3.5– 11 | 28.18 |
| ZS40.0_mf700 | Zr – O<br>Zr – O<br>Zr – Zr | 4.1<br>4.2<br>1.2 | 2.03<br>2.26<br>3.33 | 0.055<br>0.097<br>0.089 | 4.60 | 3.5– 11 | 28.53 |
| ZS20.0_mf800 | Zr – O<br>Zr – O<br>Zr – Zr | 4.0<br>4.0<br>1.0 | 2.04<br>2.26<br>3.33 | 0.063<br>0.087<br>0.087 | 4.25 | 3.5– 11 | 27.59 |
| ZS5.0_mf800 | Zr – O<br>Zr – O<br>Zr – Zr | 3.0<br>4.0<br>1.9 | 2.08<br>2.26<br>3.40 | 0.055<br>0.077<br>0.112 | 3.52 | 3.5– 11 | 24.93 |
| ZS1.3_mf700 | Zr – O<br>Zr – O<br>Zr – Zr | 3.0<br>4.0<br>2.7 | 2.09<br>2.26<br>3.41 | 0.055<br>0.081<br>0.122 | 3.35 | 3.5– 11 | 23.67 |
| $ZrO_2$(tetragonal) | Zr – O<br>Zr – O<br>Zr – Zr | 4.0<br>4.0<br>12.0 | 2.10<br>2.30<br>3.63 | 0.067<br>0.097<br>0.107 | 5.81 | 3.5– 11 | 31.16 |

[a] absorber (A) – backscatterers (Bs), [b] coordination number N, [c] interatomic distance r, [d] Debye-Waller factor σ and [e] edge position (Fermi energy) relative to calculated vacuum zero $E_f$

## 2.8 Effect of the thermal treatment

The influence of the thermal treatment, carried out with different methods on the analysed samples with a Si/Zr ratio of 5.0 and 20.0, was also performed. For the thermal treatment, a muffle and a microwave oven were used. First, the samples with a Si/Zr molar ratio of 5.0, which were annealed at 800°C, 950°C and 1000°C by using different ovens, will be discussed. The same will be done for those samples with a Si/Zr molar ratio of 20.0. Then, samples with a Si/Zr ratio of 5.0 and 20.0 annealed at 600°C, but in different ovens, will be comparatively analysed.

### 2.8.1 XANES of the samples with a Si/Zr molar ratio of 5.0

The XANES spectra of the samples ZS5.0_mf800 and ZS5.0_mw950 (figure 2.33) show apparently similar features, whereas for the sample annealed at ZS5.0_mf1000 sample at 1000°C a remarkable different behaviour is observed.
The edge width of the first two samples at low temperature is broader (see first derivatives in figure 2.34). Furthermore, the shoulder at 18.037 keV is not observed and the pre-peak at 17.993 keV typical of tetragonal $ZrO_2$ has a much smaller intensity. It can be concluded that both samples, also if they were annealed with different methods and at different temperatures, do not show any well defined features. On the other hand, the ZS5.0_mf1000 sample shows a different behaviour. From the XANES spectrum in figure 2.33 one can conclude that the local environment of this sample is similar to tetragonal $ZrO_2$. The spectrum shows the typical features to tetragonal $ZrO_2$ reference such as the shoulder at 18.037 keV and the twin peak feature of the white line but with a double peak that is less pronounced than in tetragonal $ZrO_2$, in agreement with XRD data (figure 2.27).

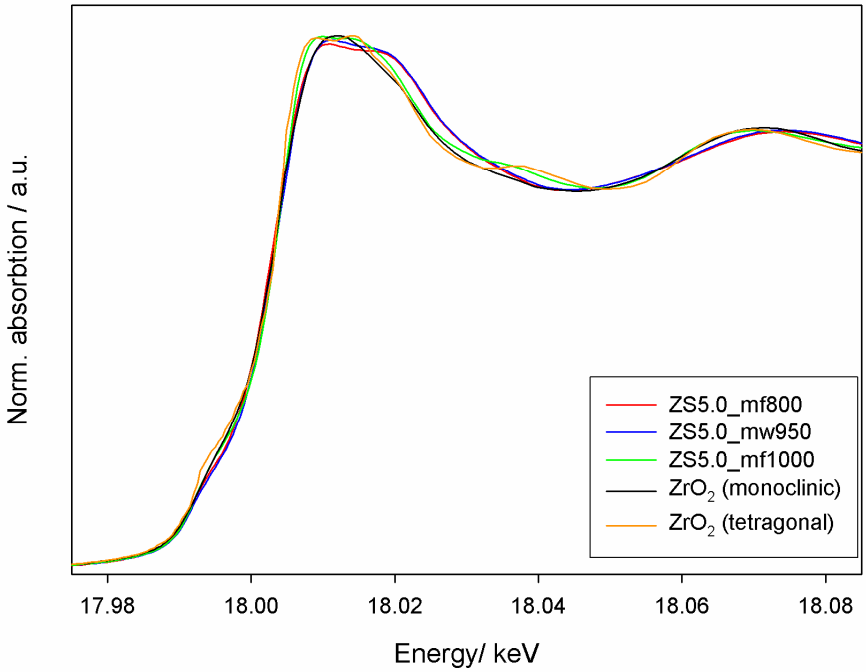


**Figure 2.33:** XANES spectra of the samples with a Si/Zr ratio of 5.0 annealed in a high range of temperature in different ovens (muffle and microwave).

Surprising are the structural differences between the sample annealed at 950°C in microwave oven and the sample annealed at 1000°C in the muffle oven. Due to the similar annealing temperature, a similar structure could have been expected. However, noticeably different features were pointed out. This may be explained by the fact that sample ZS5.0_mf1000 was annealed in the muffle oven for five hours, whereas sample ZS5.0_mw950 only for one hour in the microwave. In the latter case, the limited annealing time is too short for the phase separated $ZrO_2$ domains grow in size and to become more ordered. It should be moreover highlighted that the heating mechanism induced by microwave is completely different from the conventional annealing in muffles. This can in turn determine remarkably different structural evolution pattern in the treated materials. Furthermore, the determination of the exact temperature of a sample inside the microwave oven is difficult because the thermocouple is not directly in contact with the sample. Moreover, the temperature values during calcination are not constant but oscillates within a certain range. For high annealing temperatures, this effect is stronger. For these reasons the given temperature in the sample name is always the highest temperature shown in the oven display. Therefore, the true annealing temperature of the sample might be a bit lower.

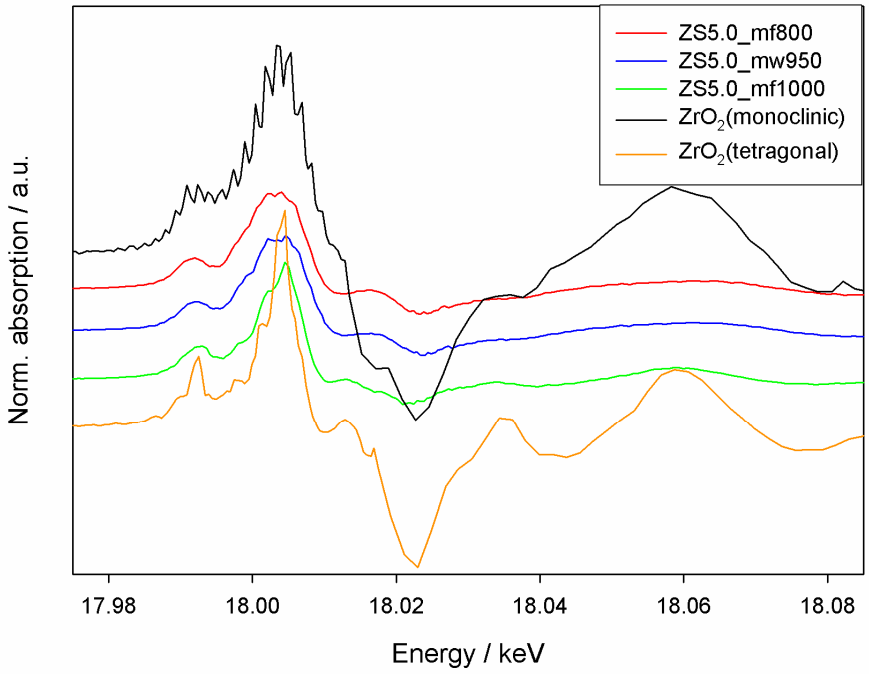


**Figure 2.34:** First derivative of the XANES spectra of the samples with a Si/Zr ratio of 5.0 annealed 800°C, 950°C and 1000°C in different ovens (muffle and microwave).

### 2.8.2 EXAFS of the samples with a Si/Zr molar ratio of 5.0

The experimental data were evaluated taking the results of the XANES investigation into account. The ZS5.0_mf800 and ZS5.0_mw950 samples were fitted with two O-shells and one Zr-shell.

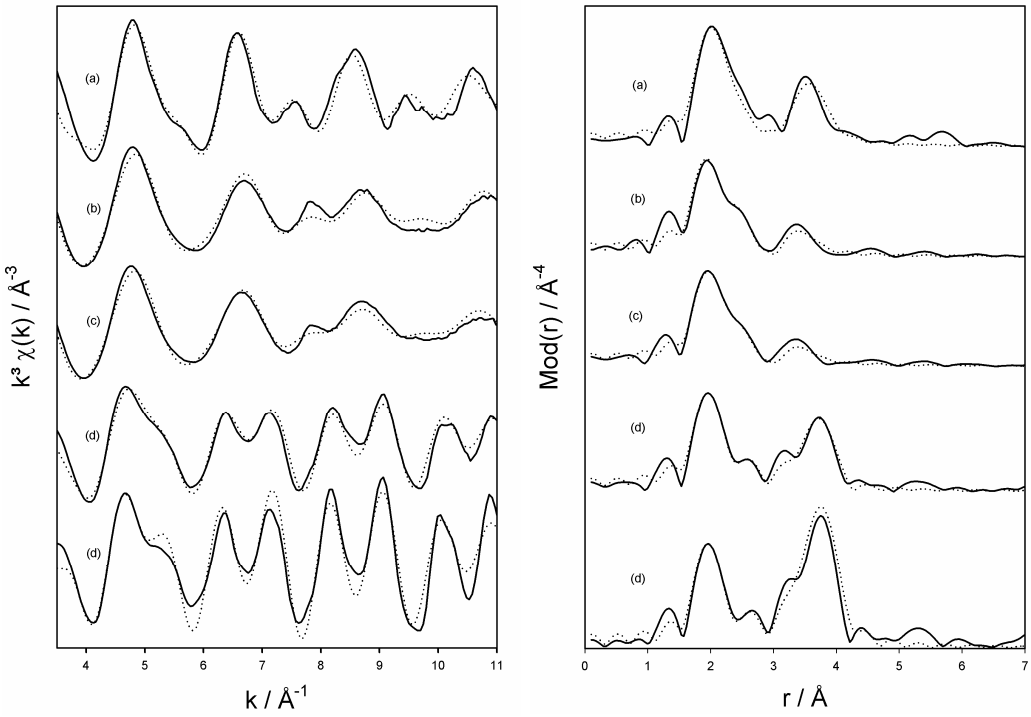


**Figure 2.35:** Experimental (solid line) and simulated (dotted line) EXAFS functions and their corresponding Fourier transforms for the samples: **(a)** monoclinic $ZrO_2$, **(b)** ZS5.0_mf800, **(c)** ZS5.0_mw950 **(d)** ZS5.0_mf1000 samples, **(e)** tetragonal $ZrO_2$.

Interestingly, the coordination number of the Zr-shell of the ZS5.0_mw950 sample is smaller than for the ZS5.0_mf800, although it should be expected that, with increasing temperature, the system become more ordered. The small decrease in the coordination number could be attributed to the fact that sample ZS5.0_mw950 was annealed for only one hour in a microwave oven, whereas sample ZS5.0_mf800 was annealed for five hours in a muffle oven and also to the already mentioned annealing process induced by microwaves. However, the difference between the coordination numbers is still within the error range.

The XANES spectrum of the ZS5.0_mf1000 sample shows features similar to the tetragonal reference: the Zr-shell distance of 3.62 Å is very close to the typical value of 3.63 Å.

Since a temperature difference of 50°C is not expected to determine significant structural changes, it can be concluded that the use of different annealing methods, muffle and microwave oven, leads to different results. This can be

ascribed to both a different mechanism of heat deposition and to the different treatment time, five hours and one hour for muffle and microwave oven, respectively. It could also be reasonable to assume that the temperature of 1000°C is responsible for the rearrangement toward the tetragonal structure. One reason for this behaviour could be, as outlined previously, that sample ZS5.0_mf1000 was annealed in a muffle oven for five hours and sample ZS5.0_mw950 only for one hour in microwave oven. In summary, it can be said that the microwave sample annealed at 950°C has a local structure which is more similar to the 800°C sample calcined in the muffle oven. Accordingly, both these samples show an amorphous diffraction pattern with broad and unsharp features (figure 2.36 a and b).

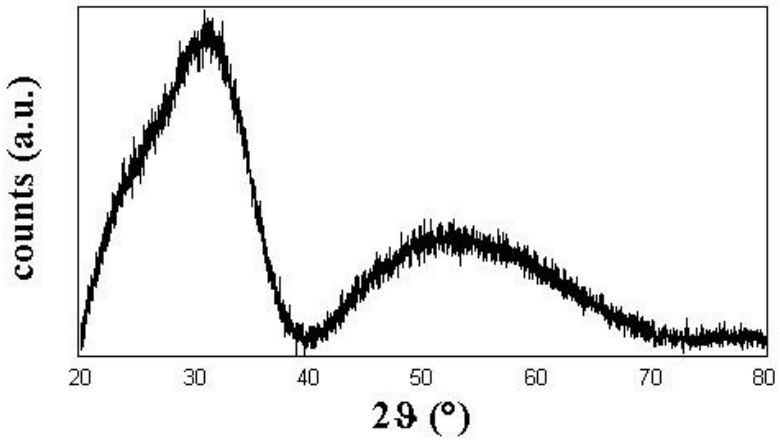


**Figure 2.36a:** XRD diffractogramm of sample ZS5.0_mf800.

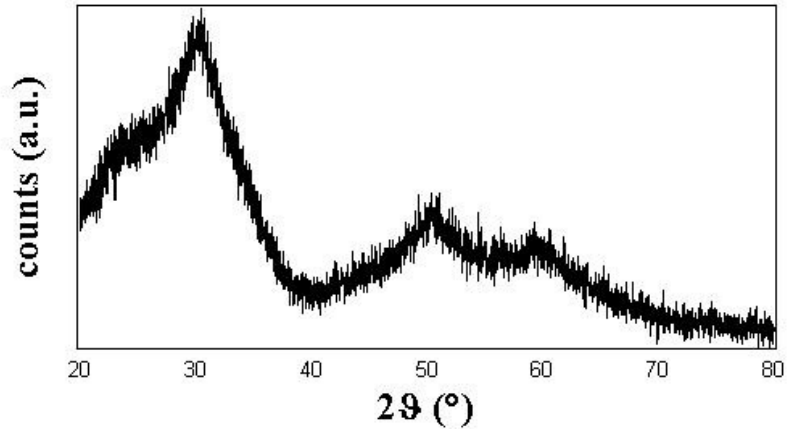


**Figure 2.36b:** XRD diffractogramm of sample ZS5.0_mw950.

**Table 2.9:** Structural parameters for the samples: **(a)** monoclinic $ZrO_2$, **(b)** ZS5.0_mf800, **(c)** ZS5.0_mw950 **(d)** ZS5.0_mf1000 samples, **(e)** tetragonal $ZrO_2$.

| | A-Bs[a] | N[b] | r[c] [Å] | σ[d] [Å] | $E_f$ [e] [eV] | k-range [$Å^{-1}$] | Fit Index |
|---|---|---|---|---|---|---|---|
| $ZrO_2$(monoclinic) | Zr – O | 3.0 | 2.08 | 0.050 | 7.23 | 3.5– 11 | 28.18 |
| | Zr – O | 4.0 | 2.23 | 0.074 | | | |
| | Zr – Zr | 7.0 | 3.48 | 0.120 | | | |
| ZS5.0_mf800 | Zr – O | 3.0 | 2.08 | 0.055 | 3.52 | 3.5– 11 | 24.93 |
| | Zr – O | 4.0 | 2.26 | 0.077 | | | |
| | Zr – Zr | 1.9 | 3.40 | 0.112 | | | |
| ZS5.0_mw950 | Zr – O | 3.0 | 2.09 | 0.059 | 3.16 | 3.5– 11 | 23.00 |
| | Zr – O | 4.0 | 2.26 | 0.084 | | | |
| | Zr – Zr | 1.6 | 3.40 | 0.116 | | | |
| ZS5.0_mf1000 | Zr – O | 4.0 | 2.10 | 0.071 | 3.51 | 3.5– 11 | 23.05 |
| | Zr – O | 4.0 | 2.30 | 0.100 | | | |
| | Zr – Zr | 3.9 | 3.62 | 0.092 | | | |
| $ZrO_2$(tetragonal) | Zr – O | 4.0 | 2.10 | 0.067 | 5.81 | 3.5– 11 | 31.16 |
| | Zr – O | 4.0 | 2.30 | 0.097 | | | |
| | Zr – Zr | 12.0 | 3.63 | 0.107 | | | |

[a] absorber (A) – backscatterers (Bs), [b] coordination number N, [c] interatomic distance r, [d] Debye-Waller factor σ and [e] edge position (Fermi energy) relative to calculated vacuum zero $E_f$

### 2.8.3 XANES of the samples with a Si/Zr molar ratio of 20.0

The XANES spectra of the samples with a Si/Zr ratio of 20.0 (figure 2.37) look similar to those of the series with a Si/Zr ratio of 5.0 but with an interesting difference: the spectra of the first two samples show a positive slope. For the ZS20.0_mf1000 sample at 1000°C, a different behaviour is observed.

The edge width of the ZS20.0_mf800 and ZS20.0_mw950 samples are similar and broader. Both samples, also if they were annealed with different methods and at different temperatures, do not show any well defined features that can be related to ordered structure. These results, ascribable to the low Zr-content, indicate that the local environment of these two samples has, as already described in paragraph 2.4.3, a contribution of $ZrO_6$ polyhedra.

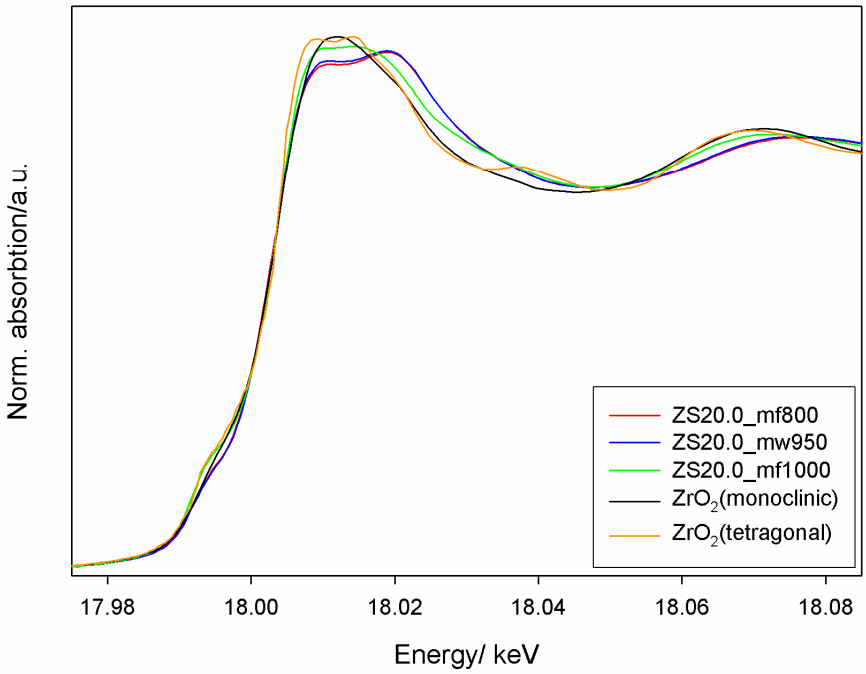


**Figure 2.37:** XANES spectra of the samples with a Si/Zr ratio of 20.0 annealed at 800 °C, 950 °C and 1000 °C in different ovens (muffle and microwave).

The ZS20.0_mf1000 sample shows a different behaviour. The white line of the ZS20.0_mf1000 sample is broader than for tetragonal zirconia. It should also be noted that for this sample the shoulder at 18.037 keV is not as pronounced as in pure tetragonal zirconia, but the spectrum exhibits an increased absorption in the same region, indicating a tetragonal local structure. In comparison, the shoulder is less emphasised than for the samples with a higher Zr-content such as ZS5.0_mf1000, ZS2.5_mf1000 and ZS1.3_mf1000. Interestingly, the pre-edge peak at 17.993 keV is very similar and shows the same intensity as the tetragonal reference. As already previously explained this can be attributed to a less centrosymmetric Zr-O geometry (see chapter 2.6.3). Summarising, one can deduce (figure 2.37) that this sample has a local environment similar to tetragonal $ZrO_2$. Also in the XRD spectrum broad tetragonal peaks can be observed (figure 2.27). This result will be confirmed by EXAFS investigation.

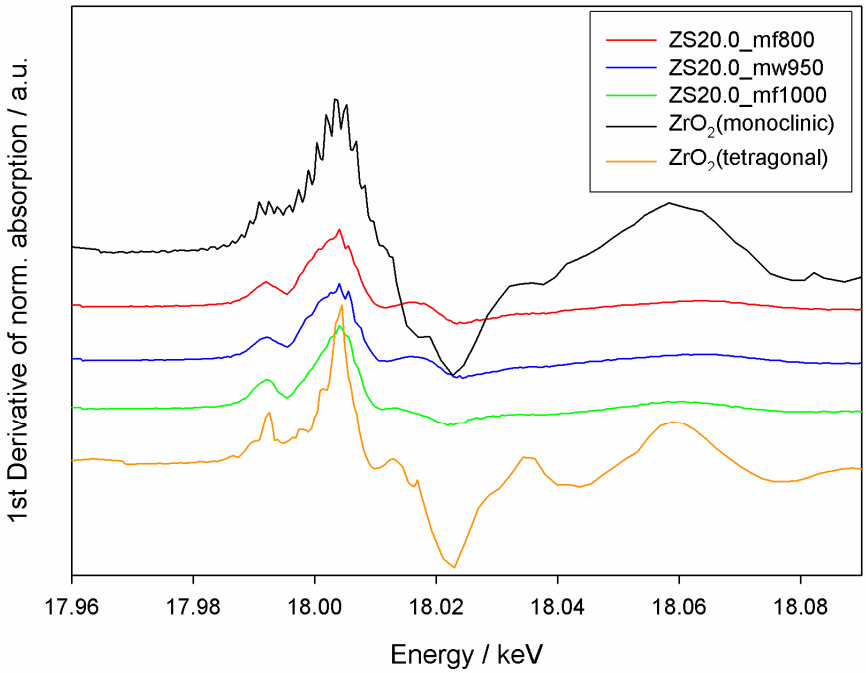


**Figure 2.38:** First derivative of the XANES spectra of the samples with a Si/Zr ratio of 20.0 annealed at 800°C, 950°C and 1000°C in different ovens (muffle and microwave).

### 2.8.4 EXAFS of the samples with a Si/Zr molar ratio of 20.0

As already observed in the previous chapter, the XANES spectra of the samples with a Si/Zr ratio of 20.0 are very similar to those of the samples with a Si/Zr ratio of 40.0. Therefore the same fitting procedure was applied. The EXAFS determined structural parameters are summarised in table 2.10. For the sample ZS20.0_mf800 and ZS20.0_mf950 the combined O-coordination of the first two shells is about 8, but as already discussed in chapter 2.8.1 the short Zr-O distances of the first O-shell (2.04 Å, 2.05 Å) obtained by EXAFS analysis could be attributed to a small contribution of $ZrO_6$ polyhedra. For both samples, the EXAFS results show a coordination number of about 1 for the Zr-shell.

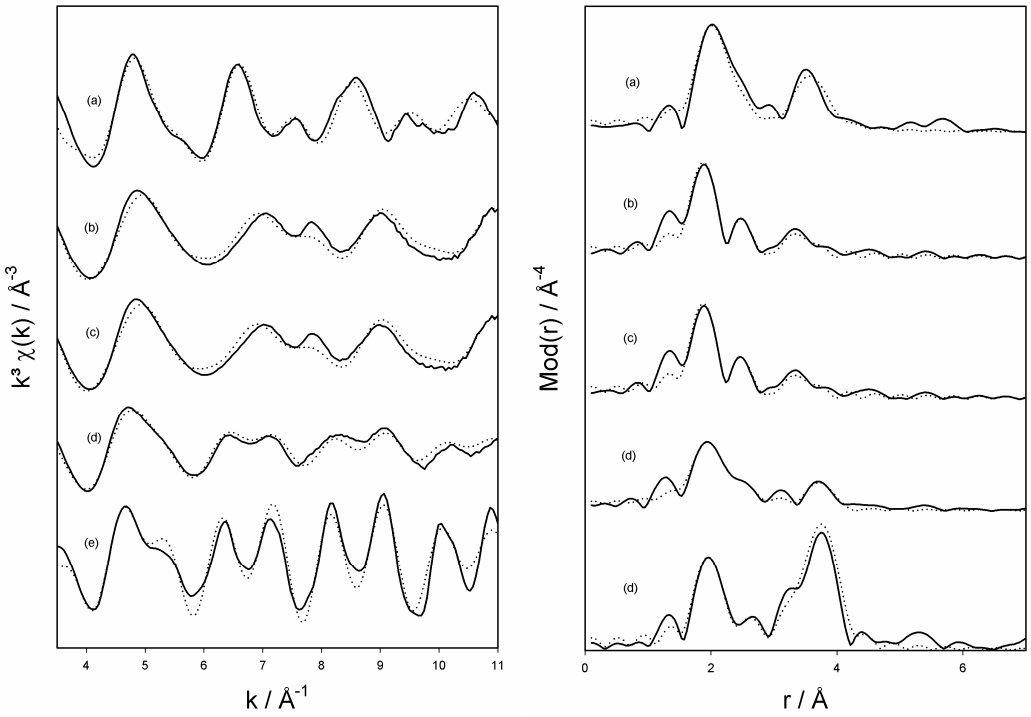


**Figure 2.39:** Experimental (solid line) and simulated (dotted line) EXAFS functions and their corresponding Fourier transforms for samples: **(a)** monoclinic $ZrO_2$, **(b)** ZS20.0_mf800, **(c)** ZS20.0_mw950, **(d)** ZS20.0_mf1000, **(e)** tetragonal $ZrO_2$.

For the ZS20.0_mf1000 sample, the XANES spectrum displays some features of the tetragonal polymorph.

The Zr-shell distance is 3.62 Å and the distance of the second O-shell is 2.28 Å. As for the sequence with a Si/Zr molar ratio of 5.0 these results indicate that heating the samples with a different annealing method, i.e. muffle or microwave, leads to different results (see remarks made in chapter 2.8.2). Also here, the structure of the microwave sample annealed at 950°C is completely different from the 1000°C sample calcined in the muffle oven. Instead its structure is more amorphous and similar to the muffle oven sample annealed at 800°C.

**Table 2.10:** Structural parameters for samples: **(a)** monoclinic $ZrO_2$, **(b)** ZS20.0_mf800, **(c)** ZS20.0_mw950 and **(d)** ZS20.0_mf1000 samples, **(e)** tetragonal $ZrO_2$.

| | A-Bs[a] | N[b] | r[c] [Å] | σ[d] [Å] | $E_f$ [e] [eV] | k-range [$Å^{-1}$] | Fit Index |
|---|---|---|---|---|---|---|---|
| $ZrO_2$(monoclinic) | Zr – O | 3.0 | 2.08 | 0.050 | 7.23 | 3.5– 11 | 28.18 |
| | Zr – O | 4.0 | 2.23 | 0.074 | | | |
| | Zr – Zr | 7.0 | 3.48 | 0.120 | | | |
| ZS20.0_mf800 | Zr – O | 4.0 | 2.04 | 0.063 | 4.25 | 3.5– 11 | 27.59 |
| | Zr – O | 4.0 | 2.26 | 0.087 | | | |
| | Zr – Zr | 1.0 | 3.33 | 0.087 | | | |
| ZS20.0_mw950 | Zr – O | 4.0 | 2.05 | 0.063 | 3.94 | 3.5– 11 | 27.91 |
| | Zr – O | 4.0 | 2.26 | 0.081 | | | |
| | Zr – Zr | 0.8 | 3.33 | 0.081 | | | |
| ZS20.0_mf1000 | Zr – O | 4.0 | 2.09 | 0.089 | 2.66 | 3.5– 11 | 29.31 |
| | Zr – O | 4.0 | 2.28 | 0.105 | | | |
| | Zr – Zr | 2.2 | 3.62 | 0.105 | | | |
| $ZrO_2$(tetragonal) | Zr – O | 4.0 | 2.10 | 0.067 | 5.81 | 3.5– 11 | 31.16 |
| | Zr – O | 4.0 | 2.30 | 0.097 | | | |
| | Zr – Zr | 12.0 | 3.63 | 0.107 | | | |

[a] absorber (A) – backscatterers (Bs), [b] coordination number N, [c] interatomic distance r, [d] Debye-Waller factor σ and [e] edge position (Fermi energy) relative to calculated vacuum zero $E_f$

### 2.8.5 XANES of the samples annealed at lower temperature (600°C)

The XANES spectra (figure 2.40) of the samples with Si/Zr ratio of 5.0 annealed at 600° C are very similar to the spectra of the samples in the previous chapter. A negative slope is detected for the samples with a Si/Zr ratio of 5.0, whereas for the samples with a Si/Zr ratio of 20.0 a positive slope is visible.

The white lines of the ZS5.0_mf600 and ZS5.0_mw600 samples are very similar to that of the ZS1.3_mf500 and ZS1.3_mf700 (chapter 2.6.1). Although the samples were annealed by using two different methods, they are almost identical (see first derivative figure 2.41). Because of the resemblance to the XANES region a similar local environment of the Zr-atoms can be assumed. Also in literature [G. Mountjoy *et al.* (2000)] the negative slope of the white line for $ZrO_2$-$SiO_2$ xerogels is correlated to similar structural parameters.

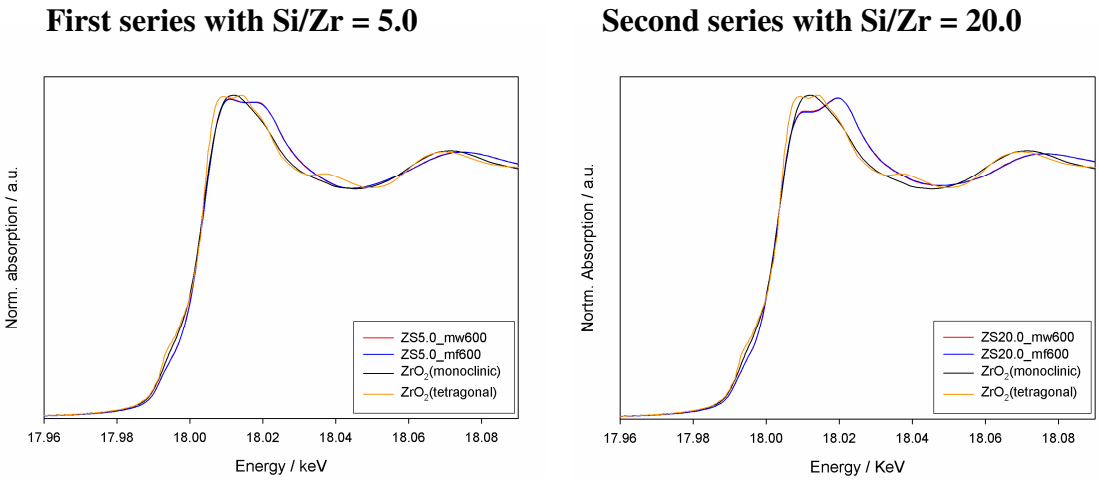


**Figure 2.40:** XANES spectra of the samples with a Si/Zr ratio of 5.0 and of 20.0 annealed at 600°C in different ovens (muffle and microwave).

The samples with a Si/Zr ratio of 20.0 show XANES spectra which are similar to those analysed in chapter 2.6.3 with a Si/Zr ratio of 40.0. Obviously, the broadness of the double peak feature of the white line can be ascribed to the higher dilution of the samples.

The positive slope of the white line, the absence of the shoulder at 18.037 keV, the weak pre-edge peak at 17.993 keV as well as the low temperature and Zr-content support the formation of disordered local systems.

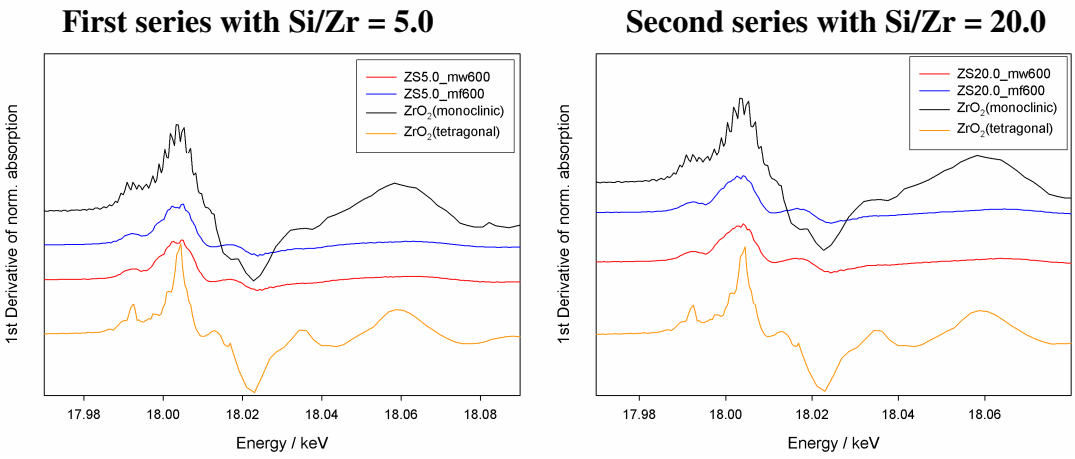


**Figure 2.41:** First derivative of XANES spectra of the samples with a Si/Zr ratio of 5.0 and 20.0 annealed at 600° C in different ovens (muffle and microwave).

It can be concluded that at 600°C, calcination in the microwave or muffle oven do not determine any remarkable difference in the local structure of the samples. This result will also be confirmed by EXAFS data analysis.

### 2.8.6 EXAFS of the samples annealed at lower temperature (600°C)

The ZS5.0_mf600 and ZS5.0_mw600 samples were fitted with two O-shells and one Zr-shell. The structural parameters determined by EXAFS are listed in table 2.11. Here, as already explained, Si-atoms in the third shell are not visible in the EXAFS signal because of their weak backscattering amplitude and their broad distribution. Additionally, the interatomic distance of the Zr-shell is not in agreement with that of pure monoclinic $ZrO_2$. This could be due to distance contraction in small particles at the interface with the silica host matrix. Also, a small amount of shorter Zr-O-Si distances could lead during fitting to smaller Zr-O-Zr distances.

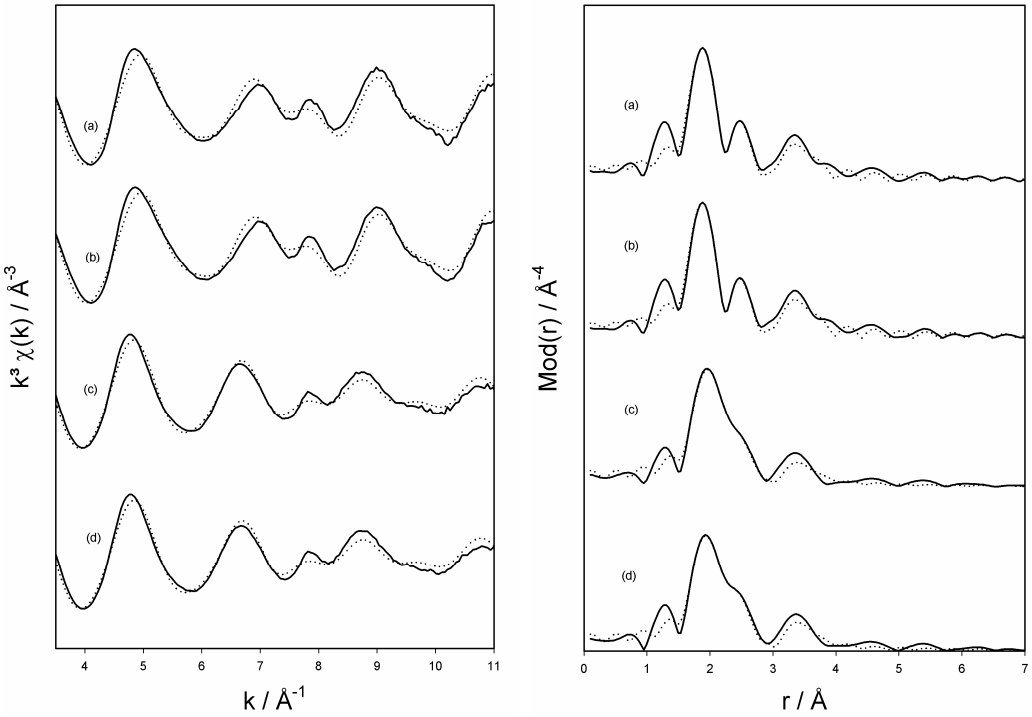


**Figure 2.42:** Experimental (solid line) and simulated (dotted line) EXAFS functions and their corresponding Fourier transforms of the samples: **(a)** ZS20.0_mw600, **(b)** ZS20.0_mf600, **(c)** ZS5.0_mw600 and **(d)** ZS5.0_mf500.

As the XANES spectra of the two samples with a Si/Zr ratio of 20.0 are very similar to those of the samples with a Si/Zr ratio of 40.0, two O-shells with coordination number of 4 and one Zr-shell was fitted. The EXAFS determined structural parameters are presented in the table 2.11. As already discussed in paragraph 2.6.4, the short Zr-O distances of the first O-shell (2.04 Å, 2.05 Å)

obtained by EXAFS analysis could be in agreement with a small contribution from $ZrO_6$ polyhedra. The coordination number of the Zr-shell is about 1.4.

As for the samples with a Si/Zr ratio of 5.0, it can be concluded that 600°C there is no difference between calcination in the microwave or muffle oven. In both cases, the formation of a disordered local structure is observed. Only at higher temperature, i.e. 950°C and 1000°C, the muffle oven samples exhibit a more ordered structure than the microwave samples.

**Table 2.11:** Structural parameters for the samples: **(a)** ZS20.0_mw600, **(b)** ZS20.0_mf600, **(c)** ZS5.0_mw600 and **(d)** ZS5.0_mf600.

| | A-Bs[a] | N[b] | r[c] [Å] | σ[d] [Å] | $E_f$ [e] [eV] | k-range [$Å^{-1}$] | Fit Index |
|---|---|---|---|---|---|---|---|
| ZS20.0_mw600 | Zr – O<br>Zr – O<br>Zr – Zr | 4.0<br>4.0<br>1.3 | 2.05<br>2.25<br>3.34 | 0.063<br>0.081<br>0.095 | 3.77 | 3.5– 11 | 27.33 |
| ZS20.0_mf600 | Zr – O<br>Zr – O<br>Zr – Zr | 4.0<br>4.0<br>1.4 | 2.05<br>2.25<br>3.34 | 0.063<br>0.081<br>0.095 | 3.88 | 3.5– 11 | 25.83 |
| ZS5.0_mw600 | Zr – O<br>Zr – O<br>Zr – Zr | 3.0<br>4.0<br>1.6 | 2.08<br>2.26<br>3.40 | 0.055<br>0.077<br>0.112 | 3.17 | 3.5– 11 | 22.26 |
| ZS5.0_mf600 | Zr – O<br>Zr – O<br>Zr – Zr | 3.0<br>4.0<br>1.8 | 2.08<br>2.26<br>3.40 | 0.059<br>0.081<br>0.116 | 3.52 | 3.5– 11 | 24.33 |

[a] absorber (A) – backscatterers (Bs), [b] coordination number N, [c] interatomic distance r, [d] Debye-Waller factor σ and [e] edge position (Fermi energy) relative to calculated vacuum zero $E_f$

# Chapter 3

## Experimental part

### 3.0 Preparation of the hybrid and oxide materials

#### Chemicals

Zirconium(IV) n-butoxide (80% in n-butanol, purchased from Strem Chemical), (methacryloxymethyl)triethoxysilane (purchased from ABCR), methacrylic acid 99%, anhydrous tetrahydrofuran and anhydrous toluene (purchased from Aldrich) were used as received and then stored under argon. The polymerisation initiator dibenzoylperoxide was purchased by Aldrich.

#### Preparation of the starting solution

Due to the high moisture- and air-sensitivity of the precursors, all preparation steps of the solutions were performed under argon using standard Schlenk techniques. The synthesis process (preparation of the solutions used for the synthesis of the gels and polymerisation) is schematically sketched in the flow chart of figure 1 and involves three different steps.

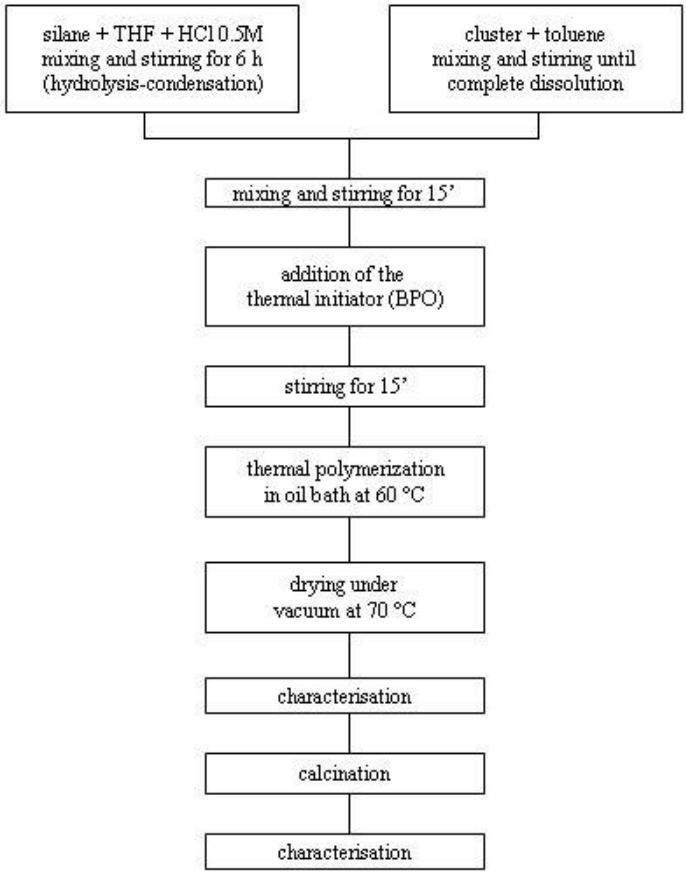


**Figure 3.1:** Flow chart of the synthetic procedure.

First, the methacryloxysilane (MAMTES) was dissolved in THF and prehydrolysed with water in the presence of HCl as catalyst for eight hours at room temperature. The prehydrolysis conditions have been previously optimised on the basis of time-resolved ATR and NMR data. Typical molar ratios in the sol–gel solution were methacryloxysilane : $H_2O$ : HCl = 1 : 4 : 0.04. The cluster $Zr_4O_2(OMc)_{12}$ was separately synthesised through a mixture of 80 wt% $Zr(O^nBu)_4$ in n-butanol solution and 7 molar equivalents of methacrylic acid (MAA) [Trimmel, G. *et al.* (2001), Gross, S. *et al.* (2003)]. A weighed amount of the crystalline cluster was dissolved in toluene and this solution was then mixed with the prehydrolysed methacryloxysilane and stirred at room temperature for fifteen minutes.

To this solution the dibenzoylperoxide was added (1% w/w with respect to the silane monomer) under stirring. The obtained solutions were heated at 60 °C until polymerisation occurred. A typical polymerisation time was about 1 h. Different

samples (see Table 2.2) were prepared by varying the methacryloxysilane : cluster molar ratio (Si/Zr molar ratio of 1.3, 2.5, 5.0, 10, 20.0, 40.0) to investigate how the different parameters affect the final compositional and microstructural features of the system.

After polymerisation, the zirconium based gels were dried under vacuum at 70°C for twelve hours to eliminate the residual solvent yielding the materials labelled as "as prepared samples" (table 2.2). A part of the prepared gels was thermally annealed at different temperatures in air to promote pyrolysis of the organic components and their conversion to the corresponding binary oxides. As reported in chapter 1, the thermal treatments were carried out by conventional and microwave oven.

The samples with Si/Zr molar ratios of 1.3 and 40.0 were annealed in a muffle oven for four hours. All other muffle oven samples were calcined for five hours. The calcination time for the microwave samples was always one hour.

**Sample preparation for EXAFS measurements**

Solid samples for EXAFS analysis were ground and pressed to pellets with a diameter of 1 – 1.3 cm diameters. In order to obtain a better stability of the pellet, it was necessary to add an inert substance such as polyethylene or cellulose. The necessary amount of substance depends on the concentration of the absorber and on the total absorption of the sample and it was chosen to achieve an overall absorption of the sample μd between 1.0 and 3.0 and a jump at the absorption edge Δμd of about 1. The prepared pellet was then glued by kapton tape to the sample holder and positioned in the beam. In the case of elementary metals, metal foils with a thickness of a few micrometers were used as reference.

### 3.1 EXAFS Beamline

The EXAFS measurements of the examined substances were performed at the beamline X1 at HASYLAB, DESY (Hamburg) at Zr K-edge at 17998 eV. The positron energy in the ring was 4.45 GeV and the beam current was about 120 mA. The samples were measured with Si (311) double crystal monochromator at the Zr K-edge. Data were collected in transmission mode with ion chambers filled with argon for Zr K-edge measurements.

### 3.2 Data analysis

The total absorption coefficients μ(E) was calculated according to the equation:

$$\mu(E) = \ln \frac{I_0(E)}{I_1(E)} \qquad (3.1)$$

For fluorescence measurements, equation 3.2 was used:

$$\mu(E) \propto \frac{I_f(E)}{I_0(E)} \qquad (3.2)$$

Here, $I_0(E)$ and $I_1(E)$ are the dark-current corrected count rates of the detectors before and after the sample. $I_f(E)$ is the count rate of the fluorescence detector.

Since during EXAFS analysis only the energy difference relative to the absorption edge is considered, an exact energy calibration is not necessary. However, for the comparison of the XANES spectra of different samples, an exact determination of the edge position is mandatory. This is done by using the well-known edge position of a reference sample (see figure 2.6), generally a metal foil of the considered element which is measured between the second and third ionization chamber.

For the normalisation and transformation into k-space of an EXAFS function, it is necessary to know the relative position of the absorption edge ($E_0$). This can be determined either with WINXAS or with the program EXRD by T. S. Ertel [T. S. Ertel, T. S. *et al.* (1992)]. If EXRD is used, then two different procedures can be selected: by using "the inflection point method", $E_0$ is determined from the position of the first inflection point within the absorption edge. The other possibility is the so-called "convolution method", which determines the common intersection of the experimental spectrum and a set of functions, which result from multiplication of the experimental spectrum with standardised gaussian distribution functions of different half widths [Boland, J. J. *et a.l.* (1983)]. The $E_0$-energies obtained in such a way deviate only by a few eV from the true ionization energies.
Since the normalization of the spectra was done with WINXAS, the so determined $E_0$-values were used. For the background correction with AUTOBK the $E_0$-value was selected, which lay best within the edge.

The detected total absorption consists of the absorption edge of the absorber and the basic absorption, which is caused by Compton scattering, absorption edges of lower energy and other physical effects [Teo, B.K. *et al.* (1986)]. This basic absorption can be removed from the total absorption by fitting to the pre-edge region a Victoreen polynomial [Victoreen, J. A. *J. et al.* (1948), Victoreen, J. A. *et al.* (1943), Victoreen, J. A. *et al.* (1949)] and by extrapolation over the entire data range.

$$\mu_v(E) = A \cdot E^{-3} + B \cdot E^{-4} \qquad (3.3)$$

Here, A and B are constants, which are determined during the fitting of the polynomial. By subtraction of the Victoreen function from the total absorption coefficient the "true" absorption coefficients $\mu_t(E)$ is finally obtained:

$$\mu_t(E) = \mu(E) - \mu_v(E) \qquad (3.4)$$

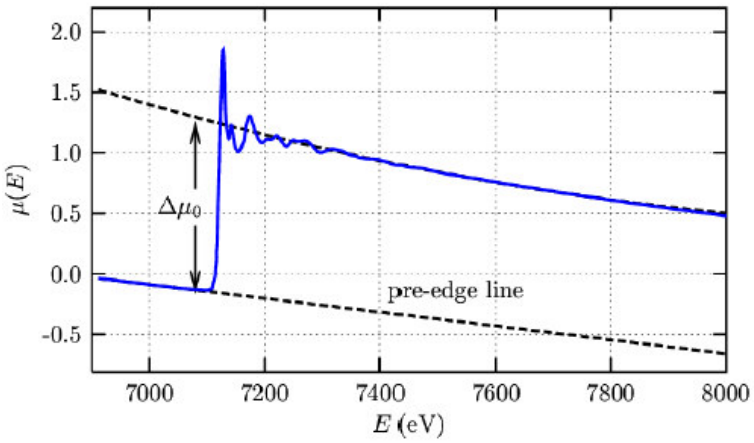


**Figure 3.2:** Pre-Edge Subtraction. The background that fits the *pre-edge* region is subtracted away. This gets rid of the absorption due to other edges.

During the following normalization, a polynomial of 0th order (y = const) is fitted to the post-edge region of the spectrum. By dividing $\mu_t(E)$ by *const* the normalized spectrum with an edge jump of 1 is obtained

$$\mu_n(E) = \frac{\mu_t(E)}{const} \qquad (3.5)$$

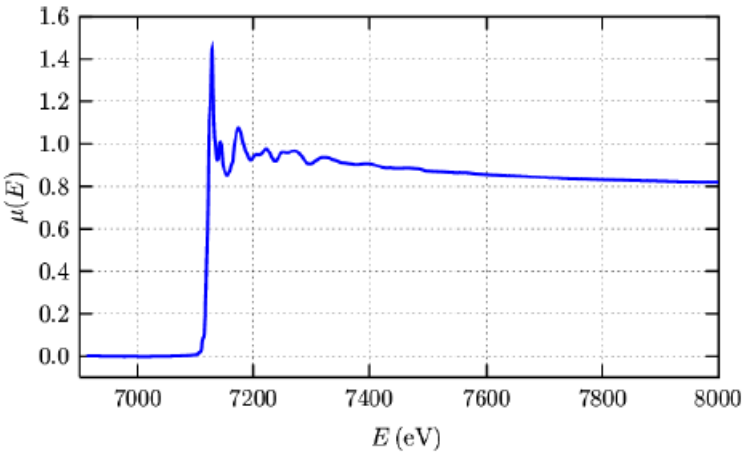


**Figure 3.3:** The *edge step*, $\mu_0(E_0)$, is estimated by extrapolating a simple fit to the above μ(E) to the edge. The normalisation is done by this value to get an edge jump of 1.

### 3.3 Interpretation of the spectra

The EXAFS spectra can be examined by Fourier transformation of the $\chi(k)$ function into r-space. This provides a modified radial distribution function, whose maxima can be assigned to individual backscatterers. However, for complicated systems with maxima at similar distances, it is necessary to use Curve fitting of the experimental spectrum[Koningsberger, D. C *et al.* (1988), Teo, B.K. *et al.* (1986)] with theoretical function based on the variation of the structural parameters.

Moreover, because there is more than one structural model which sufficiently describes the experimental spectrum, it was necessary to use additional information, such as structural models or crystallographic data. With exact knowledge of the coordination geometry, the coordination numbers can be fixed to the known values while iterating the other parameters. Another possibility is to set limits for the parameters within which they may be varied.

In this work, all $\chi(k)$ functions were weighted with $k^3$. The simulation of the experimental spectra was performed with the program Excurve 98 using Curved Wave theory and single scattering. For each shell the interatomic distance r between central atom and backscatterer, the coordination number N, the Debye Waller factor and an energy shift $E_f$ (valid for all shells) were fitted. For the calculation of the potential and phase shift functions, Xalpha potentials were used.

# Chapter 4

## Conclusion

EXAFS and XANES spectroscopic analysis have been performed at the Zr K-edge (17998 eV) on $ZrO_2$–$SiO_2$ binary oxides. The synthesis of the samples was performed in the working group of Professor Tondello in the "Dipartimento di scienze chimiche" of Padova using an experimental strategy which involves the use of methacryloxy-functinalised silanes and a sol-gel/polymerization two-step process. This method is well suited for preparation of homogeneous multicomponent gels, which, upon calcination, evolve to give the corresponding binary oxides, i.e. $ZrO_2$–$SiO_2$.

In the case of the samples with a Si/Zr ratio of 1.3 the XANES spectra exhibited at lower temperatures features similar to monoclinic $ZrO_2$ and due to this resemblance it can be pointed out that the local environment of the zirconia atoms is similar to the monoclinic reference. The EXAFS results confirmed this behavior. In fact, the obtained structural parameters show a more disordered coordination of the low temperature samples, which is in agreement with this reference. On the other hand, for the two samples at higher temperatures the XANES spectra reveal a coordination geometry of the Zr-atoms that is similar to tetragonal $ZrO_2$. For these samples the EXAFS obtained parameters are also in agreement with those of the tetragonal reference and the formation of small $ZrO_2$ domains with a local structure similar to tetragonal zirconia can be assumed. These results were confirmed by the corresponding XRD spectra.

For the samples series with a Si/Zr molar ratio of 40.0 the XANES spectra show results that indicate a local environment neither similar to the monoclinic nor to the tetragonal polymorph. A completely disordered phase is rather appropriate to describe the local environment. These results are in accordance with the small amount of zirconium atoms incorporated in the silica matrix. Also EXAFS analysis indicates the formation of an amorphous structure different from monoclinic and tetragonal $ZrO_2$.

The samples with different Si/Zr molar ratios annealed at 1000°C exhibit in the XANES region typical features of the tetragonal $ZrO_2$, which are more

pronounced as the Zr-concentration is increased. Especially, at high concentration, a local environment similar to tetragonal $ZrO_2$ is present. Solely the sample with a Si/Zr molar ratio of 40.0 is better described with an amorphous structure model. From the EXAFS analysis the obtained parameters are identical with those of the tetragonal $ZrO_2$ and only slightly different distances were found. Also, EXAFS results show that for the sample with a low Zr-content an amorphous structure different from tetragonal $ZrO_2$ can be assumed. These results were also evidenced by XRD analysis.

For the samples with a Si/Zr molar ratio of annealed at lower temperatures, i.e. 500°C, 600°C, 700°C, 800°C, the XANES spectra indicate that the local environment of samples with a higher Zr-content is similar to that of the monoclinic polymorph rather than the tetragonal one, whereas the formation of an amorphous structure different from monoclinic and tetragonal zirconia is found for the four samples with a smaller Zr-content. The structural parameters of the not concentrated samples obtained from EXAFS analysis are also in good agreement with the monoclinic reference.

The XANES spectra of the samples with a Si/Zr molar ratio of 5.0 and 20.0 annealed in different ovens (microwave and muffle) exhibit the same behaviour. The two samples annealed at 800°C do not show any well defined features of the tetragonal $ZrO_2$ in the XANES spectra and also EXAFS analysis confirms amorphous structure of these samples. The samples calcined at 1000°C in the muffle oven exhibit a local structure similar to tetragonal $ZrO_2$. Surprisingly, the samples annealed at 950°C in the microwave oven show a different structure. The local environment is more disordered and comparable to the 800°C muffle oven samples. This could be attributed to the fact that the annealing time was only one hour for the microwave samples and five hours for the muffle oven samples.

The samples annealed at 600°C in muffle and microwave ovens do not show any differences. Both, XANES and EXAFS analysis indicate that the two series have a disordered structure better described with an amorphous local environment.

# Ringraziamenti

Desidero ringraziare il Prof. Tondello per avermi dato la possibilità di svolgere questo lavoro di tesi, il Prof. Bertagnolli per avermi assistito durante il mio internato di tesi presso l'università di Stuttgart, la Dott.ssa Silvia Gross per avermi dato l'opportunità di svolgere la tesi in Erasmus, la Prof.ssa Anna Lisa Maniero per l'interesse dimostratomi, il Prof. Klaus Muller, il mio tutor a Stuttgart Eric Wendel per avermi sopportato così bene, Matthias Bauer per i suoi infiniti aiuti e tutto il gruppo di ricerca dell'università di Stuttgart per avermi fatto sentire come a casa.

Sono poi molte le persone che devo ringraziare sia per questo lavoro sia per questi anni universitari. È stata anche la loro presenza e i loro consigli che mi hanno permesso di raggiungere questo traguardo importante che altro non è che un punto di partenza. Comincio innanzitutto dalla mia famiglia, i miei genitori Lino e Madalisa (non ci sono parole per esprimere quello che avete fatto finora), mia sorella Sabina (un grazie sarebbe riduttivo), Paolo, mio fratello Diego (sempre presente anche se lontano…), le mie nipoti Anna ed Eleonora, mia zia Gianna (una presenza insostituibile), mio zio Angin, i miei nonni e Giorgia (se solo potessi leggere i miei pensieri capiresti cosa significhi per me).

Giovanni (senza del quale questo lavoro non avrebbe preso forma cartacea).

Tutti gli amici di Asolo, Luca, Gino, Giacomo, Rosti, Franco, Dino, Paolino, Canil, Baggio, Nicoletta, le cameriere dell'Epoca, Umberto Lisiero, Martina e Ingrid Molino, Prudente, Martina, Gigi il bocia, Simonetti.

L'appartamento di riviera Pal, Francy Chang, Giantonio: Giantonio (just older), Lucchini (un maestro), Pozza, Marigo (re scorpione), Carrera, Mirko, Bort, Canova, Valeria e Alessandra, Silvia Rossa, Anna Piuzzi, Sara, Valle, Dario (la lucidità che mi ha sempre affiancato), Zanon, Ale, Moby, Javi Bibao, Lamanuzzi (fenomeno), Silvia Gross (nuovamente, in quanto non è stata solo una correlatrice ma anche un'amica), Simone Mascotto, Pescarolo, Rosolino (Pierdimenico), Giorgio, Tito (un sostegno indescrivibile), Chiara, il Pettino, Cinzia, Silvia,

Bastien (mi ha fatto sentire poco la mancanza di casa, soprattutto nelle prime settimane di erasmus…let's go party to Schocken), Wissem, Luciano (..e che te lo dico a fa'), Fabio (eins), Giovanni, Stefano, Francesca Donini, Arda, Pegor, Jules, Lorenzo, Lara, Lydie, Linda, Aistee e tutti quelli che ho conosciuto in erasmus (compresi i soliti ingnoti che mi hanno svaligiato il frigo), il primo appartamento in arcella, l'appartamento in via Annibale Padovano e quello attuale, Maurizio Cuna, Floriano e il pollaio, la città di Stoccarda e tutti i ricordi ad essa legati, Amburgo, il Liviano e tutti quelli che ho dimenticato qui, ma non nel mio cuore…vedete, è difficile dire così tanto in così poco a così tante persone ma se un uomo può essere giudicato dagli amici che ha, allora io sono il più fortunato che esista.

J. Bon Jovi, R. Sambora, T. Torres, D. Bryan (they are the soundtrack of my life), Skid row, Guns n' Roses, L.A. Guns, Smashing Pumpkins, Bryan Adams, Desmond Child, Aerosmith, AC/CDC (lunga vita al rock 'n roll), Mättheus, Brheme, Materazzi, Giuliano Palma, Marlene Kuntz, i Sottosonico, i Tokyo Hotel (durch den Monsun), Ermes (Mercurio o Hg), le finestre del dipartimento di chimica, il quartiere Reeperbahn, il sincrotrone che con la sua luce mi ha indicato la via, l'HLX (..indimenticabile l'avaria in aereo), il generale Lee, Mirco buso, Coppola, Riello, Mac Gyver, gli spritz, Gino Cinello, l'Asolo calcio, Salvo e la sua corrida, il beach volley.

# Bibliography


Armelao, L.; Bertagnolli, H.; Gross, S.; Krishnan, V.; Lavrencic-Stangar, U.; Müller, K.; Orel, B.; Srinivasan, G.; Tondello, E.; Zattin, A. (2005) *J. Mater. Chem*. **15**, 1954

Bart, J. C. J. (1986) *Adv. Catal.* **34**, 283

Bertagnolli, H.; Teja, S. E. (1994) *Angew. Chem. Int. Ed. Engl*. **33**, 45

Boland, J. J.; Halaka, F. G.; Baldeschwieler, J. D. (1983) *Phys. Rev. B* **28,** 2921

Bosman, H.J.M.; Kruissink, E.C.; Vanderspoel, J.; Vanderbrink, F. (1994) *J. Catal.* **181**, 285

Brinker, C. J.; Scherer, G. W. (1990) *Sol-Gel Science: The Physics and Chemistry of Sol-Gel Processing,* Academic Press Inc., San Diego

Dang, Z.; Anderson, G.B.; Amenomya, Y.; Morrow, B.A. (1995) *J. Phys. Chem.* **99**, 14437

De Boor, C. (1978) *A practical guide to splines* (Springer Verlag, New York)

Ertel, T. S.; Bertagnolli, H.; Hückmann, S.; Kolb, U.; Peter, D. (1992) *Appl. Spectrosc.* **46,** 690

Evans, A. M.; Williamson, J. P. H: , Glasser, F. P. (1980) *J. Mater. Sci.* **15**, 1765

Farges, F.; Brown Jr., W. G. E.; Rehr, J. J. (1997) *Physical Rev. B,* **56,** 1809

Farges, F.; Ponader, C.; Brown Jr., W. G. E. (1991) *Geochim. Cosmochim. Acta*, **55**, 1563

Feng, Z.; Postula, W. S.; Erkey, C.; Philip, C. V.; Akgerman, A.; Anthony, R. G. (1994) *J. Catal.* **148**, 660

Feth, M. (2003) *Dissertation, Universität Stuttgart, 2003*

Fontaine, A.; Dartyge, EItie, J.P., Fucha, A.; Polain, A., H. Tolentino, Tourillon, G. Top. (1989) *Curr. Chem.* **151**, 179

Frahm, R., (1989) *Physica B* **158**, 342

*Gmelins Handbuch der anorganischen Chemie* (1973)Verlag Chemie, Weinheim, Band 42, Zr

Gross, S; Trimmel, G.; Schubert, U.; Di Noto, V. (2002) *Polym. Adv. Technol.* **13**, 254

Gross, S.; Kickelbick, G.; Puchberger, M.; Schubert, U. (2003) *Monatshefte für Chemie* **134**, 1053

Gurman, S.J.; Binstead, N.; Ross, I. (1986) *J. Phys. C.* **19**, 1845

Gurman, S. J. in *Applications of Synchrotron Radiation*, Hrsg: C. R. A. Catlow, G. N. Greaves (Blackie and Son Ltd., London, **1990**)

Hagelstein, M.; Cunis, S.; Frahm, R.; Niemann, W.; Rabe, P. (1989) *Physica B* **158**, 324

Hazen, R. M.; Finger, L. W. (1979) *J. Am. Mineral.* **64**, 157

Itoh, M.; Hattori, H.; Tanabe, K.J. (1974) *J. Catalysis* **35**, 225

Jo, H.; Blum, F. D. (1999) *Chem. Mater. J.* **10**, 2074

Kamya, K.; Sakka, S.; Tatemichi, Y. (1980) *J. Mater. Sci.* ***15***, 1765

Kickelbick, G.; Feth, M. P.; Bertagnolli, H.; Puchberger, M.; Holzinger, D.; Gross, S. (2002) *J. Chem. Soc., Dalton Trans.* 3892

Kickelbick, G. (2003) *Prog. Polym. Sci.* **28**, 83

Koningberger, D.C.; Prins, R. (1988) *X-Ray Absorption: Principles, Applications, Techniques of EXAFS, SEXAFS and XANES*, Chem. Anal. 92, Wiley, New York

Krishnan, V.; Feth, M.; Wendel, E.; Chen, Y.; Hanack, M.; Bertagnolli, H.; (2004) *Z. Phys. Chem.* **1**, 218

Lee, P. A. ; Citrin, P. H.; Eisenberger, P.; Kincaid, B. M. (1981) *Rev. Mod. Phys.* **53**, 769

Lee, P. A. ; Pendry, J. B. 1975 *Phys. Rev. B* **11**, 2795

Li, P.; Chen, I-W.; Penner-Hahn, J. E., Chang, F. (1993) *Phys. Rev. B*, **48**, 10063

Loy, D. A. (2001) *MRS Bull.* 364

Lopez, T.; Tzopantzi, T.; Navarrete, J.; Gomez, R.; Boldù, L.; Munoz, E.; Novaro, O. (1999) *J. Catal.* **181**, 285

Lytle, F.W.; Sayers, E.A.; Stern, E.A. (1975) *Phys. Rev. B* **11**, 4825

McKale, A. G.; Knapp, G. S.; Chan, S. K. (1986) *Phys. Rev. B*, **33,** 841

McKale, A. G.; Veal, B. W.; Paulikas, A. P. S.; Chan, K.; Knapp, G. S. (1988) *J. Am. Chem. Soc.* **110,** 3763

Mendez-Vivar, J.; Mendoza-Serna, R.; Valdez-Castro (2001) *J. Non-Cryst. Solids* **288**, 200

Miller, J.B.; Ko, E.I. (1996) *J. Catal.* **159**, 58

Miller, J.B.; Ko, E.I. (1997) *Catal. Today* **35**, 269

Moon, S.C.; Fujino , M.; Yamashita, H.; Anpo, M. (1997) *J. Phys.Chem.* **101**, 369

Mountjoy, G.; Anderson, R.; Newport, R. J.; Smith, M. E. (2000) *J. Physics Condens. Matter* **12**, 3505

Mountjoy, G.; Pickup D. M.; Anderson, R.; Wallidge G. W.; Holland M. A.; Newport, R. J; Smith, M. E. (2000) *Phys. Chem. Chem. Phys.* **2**, 2455

Nass, R.; Schmidt, H. (1990) *SPIE Sol-Gel Optics* **1328**, 258

Neumayer, D.A.; Cartier, E. J. (2001) *Appl. Phys.* **90**, 1801

Newville, M.; Livins, P.; Yakoby, Y.; Rehr, J. J.; Stern, E. A. (1993) *Phys. Rev. B* **47**, 14126

Nogami, M. (1985) *J. Non-Cryst. Solids* **69**, 415

Park, O.K.; Jung, J.I.; Bae, B.S. (2001) *J. Mater. Res*. **16**, 2143

Peter, D. (1993) *Dissertation*, Universität Würzburg, **1993**

Press, W. H.; Flannery, B. P.; Teukolsky, S. A.; Vetterling, W. T. (1989) *Numerical recipes* (Cambridge University Press, Cambridge)

Ressler, T. (1997) *J. de Phys. IV*, **C2-7**, 269

Sanchez, C.; In, M.J. (1992) *J. Non Cryst. Solids* **147-148**, 1

Sanchez, C.; In, M.J.; Toledano, P.; Griesemar, G. (1992) *Mater. Res. Soc. Symp. Proc.,* **271**, 669

Sanchez, C. ; Ribot, F. (1993) *J. Phys*. **3,** 1349

Sanchez, C. ; Ribot, F.; Lebeau, B. (1999) *J. Mater. Chem.* **9,** 35

Sayers, D.E.; Stern, E.A.; Lytle, F.W. (1971) *Phys. Rev. Lett*. ***27***, 1204

Stern, D. E. Sayers, F. W. Lytle, *Phys. Rev. B* (1975), **11**, 4836

Sharp, K. G.; (1998) *Adv. Mater.* **10**, 1243

Schubert, U.; Huesing, N. (2004) *Synthesis of inorganic materials,*WileyVHC, Verlag, Weinheim, 2nd edition

Simhan, R.G. (1983) *J. Non-Cryst. Solids* **54**, 335

Spanhel, L.; Popall, M.; Müller, G. (1995) *Proc. Indian Acad. Sci.: Chem. Sci.* 1995, **107**, 637

Soled, S.; McVicker, G.B. (1992) *Catal. Today* **14**, 189

Soppera, O.; Croutxè-Barghorn, C.; Carrè, C.; Blanc, D. (2002) *Appl. Surf. Sci.* **186**, 91

Srivastava, U. C.; Nigam, H. L. (1973) *Coord. Chem. Rev*. **9,** 275

Stern, E.A. (1974) *Phys. Rev. B* **10**, 3027

Stout, G. H.; Jensen, L.H. (1989) *X-Ray Structure Determination*, Wiley, New York

Teo, B.K.; Lee, P.A. (1979) *J. Am. Chem. Soc.* **101**, 2815

Teo, B.K. (1986) *EXAFS principles and data analysis*, Springer, Berlin

Terry, K.W.; Lugmair, C.G.; Tilley, T.D (1997) *J. Am. Chem. Soc.* **119**, 9745

Thulke, W.; Haensel, R.; Rabe, P. (1983) *Rev. Sci. Instrum.* **54,** 277

Trimmel, G.; Gross, S.; Kickelbick, G.; Schubert, U. (2001) *Appl. Organom. Chem.* **15**, 410

Turrillas, X.; Barnes, P.; Dent, A. J.; Jones, S. L.; Norman, C. J. (1993) *J. Mater. Chem.* **3**, 583

Wen, J.; Wilkes, G. L. (1996) *Chem. Mater.* **8,** 1667

Victoreen, J. A. (1943) *J. Appl. Phys.* **14,** 95

Victoreen, J. A. (1948) *J. Appl. Phys.* **18,** 855

Victoreen, J. A. (1949) *J. Appl. Phys.* **20,** 1141

Vlaic, G.; Olivi, L. (2004) *Croatica Chemica Acta* **77**, 427

Zandiehnadem, F. ; Murray, R. A.; Ching, W. Y. (1988) *Physica B* **150,** 19